The ESCRT protein CHMP5 restricts bone formation by controlling endolysosome-mitochondrion-mediated cell senescence

Fan Zhang[1,2,3,#], Yuan Wang[1,2,#], Luyang Zhang[1,2], Chunjie Wang[1,2], Deping Chen[4], Haibo Liu[5], Ren Xu[6], Cole M. Haynes[5], Jae-Hyuck Shim[7], Xianpeng Ge[1,2]

[1]Xuanwu Hospital Capital Medical University, Beijing, China;

[2]National Clinical Research Center for Geriatric Diseases, Beijing, China;

[3]Joint Therapeutics Co. Ltd., Beijing, China;

[4]Beijing Citident Hospital of Stomatology, Beijing, China;

[5]Department of Molecular, Cell and Cancer Biology, University of Massachusetts Chan Medical School, Worcester, Massachusetts, USA;

[6]The First Affiliated Hospital of Xiamen University-ICMRS Collaborating Center for Skeletal Stem Cells, State Key Laboratory of Cellular Stress Biology, Faculty of Medicine and Life Sciences, School of Medicine, Xiamen University, Xiamen, China;

[7]Department of Medicine/Division of Rheumatology, University of Massachusetts Chan Medical School, Worcester, Massachusetts, USA;

[#]These authors contributed equally to this work.

Correspondence to Xianpeng Ge or Jae-Hyuck Shim

Email: xianpeng.ge@xwhosp.org, xpge@penggegroup.com

or Jaehyuck.shim@umassmed.edu

Abstract

The dysfunction of the cellular endolysosomal pathway, such as in lysosomal storage diseases, can cause severe musculoskeletal disorders. However, how endolysosomal dysfunction causes musculoskeletal abnormalities remains poorly understood, limiting therapeutic options. Here, we report that CHMP5, a member of the endosomal sorting complex required for transport (ESCRT)-III protein family, is essential to maintain the endolysosomal pathway and regulate bone formation in osteogenic lineage cells. Genetic ablation of *Chmp5* in mouse osteogenic cells increases bone formation in vivo and in vitro. Mechanistically, *Chmp5* deletion causes endolysosomal dysfunction by decreasing the VPS4A protein, and CHMP5 overexpression is sufficient to increase the VPS4A protein. Subsequently, endolysosomal dysfunction disturbs mitochondrial functions and increases mitochondrial ROS, ultimately resulting in skeletal cell senescence. Senescent skeletal cells cause abnormal bone formation by combining cell-autonomous and paracrine actions. Importantly, the elimination of senescent cells using senolytic drugs can alleviate musculoskeletal abnormalities in *Chmp5* conditional knockout mice. Therefore, our results show that cell senescence represents an underpinning mechanism and a therapeutic target for musculoskeletal disorders caused by the aberrant endolysosomal pathway, such as in lysosomal storage diseases. These results also uncover the function and mechanism of CHMP5 in the regulation of cell senescence by affecting the endolysosomal-mitochondrial pathway.

Introduction

The endosomal sorting complex required for transport (ESCRT) machinery is an evolutionarily conserved molecular mechanism essential for diverse cell biological processes. Since it was initially discovered in the early 21st century in the budding yeast *Saccharomyces cerevisiae*, the molecular gear has been extensively dissected in the endocytic pathway, which sorts ubiquitinated membrane proteins and bound cargoes that commit to lysosomal degradation [1-4]. In addition to the endocytic process, ESCRT proteins also play critical roles in other cell activities, such as exocytosis, viral budding, cytokinesis, pruning of neurons, repair of the plasma membrane, and assembly of the nuclear envelope [2, 4]. In the endocytic pathway, the ESCRT machinery consists of a series of functionally overlapping protein complexes, including ESCRT-0, -I, -II and -III. While the ESCRT-0, -I, and -II complexes are mainly responsible for protein sorting and recruiting ESCRT-III components, the ESCRT-III complex, cooperating with the ATPase VPS4, is the primary executor of membrane severing during the formation of multivesicular bodies (MVB) [3, 5], which ultimately fuse with the lysosomes for cargo degradation or with the plasma membrane to release cargos into the extracellular space.

Charged multivesicular body protein 5 (CHMP5), the mammalian ortholog of yeast VPS60/MOS10, is a component of the ESCRT-III protein complex and plays an essential role in the late stage of MVB formation [6]. As the yeast *Vps60/Mos10*-null mutation disturbs the endosome-to-vacuole (the lysosome-like structure in yeast) trafficking and affects the sorting of internalized endocytic markers [7], ablation of *Chmp5* in mouse embryonic fibroblasts (MEFs) also affects the sorting from late endosomes/MVBs to lysosomes and reduces lysosomal degradation of multiple activated receptors [6]. Notably, in mouse osteoclasts, CHMP5

64 suppresses ubiquitylation of the IκBα protein and restricts the activity of NFκB pathway, without
65 any effect on endolysosomal functions [8]. During αβ T lymphocyte development, CHMP5
66 promotes thymocyte survival by stabilizing the pro-survival protein of BCL2 and does not have
67 an influence on the endolysosomal system [9]. These studies suggest that the regulation of the
68 endolysosomal pathway by CHMP5 depends on the cell and tissue context.
69
70 The dysfunction of the endolysosomal pathway can cause severe musculoskeletal disorders.
71 A such example is lysosomal storge diseases, which include more than 50 different subgroups
72 of diseases due to mutations in genes that encode lysosomal hydrolases or genes that are
73 responsible for the transport, maturation, and functions of lysosomal hydrolases [10].
74 Musculoskeletal pathologies, such as joint stiffness/contracture, bone deformation, muscular
75 atrophy, short stature, and decreased mobility, are among the most common, in some cases the
76 earliest, clinical presentations of lysosomal storage diseases [11, 12]. These musculoskeletal
77 lesions are particularly refractory to current treatments for lysosomal storage diseases, including
78 enzyme replacement treatment and hematopoietic stem cell transplantation [13]. Therefore,
79 studies on the mechanisms of musculoskeletal pathologies due to endolysosomal dysfunction
80 are paramount to design and develop novel treatments for these disorders.
81
82 In this study, our results uncover the function and mechanism of CHMP5 in the regulation
83 of cell senescence and bone formation in osteogenic cells. Deletion of *Chmp5* causes
84 endolysosomal dysfunction involving decreased VPS4A protein and subsequently activates cell
85 senescence by increasing intracellular mitochondrial ROS. Senescent cells induce bone

86 formation in both autonomous and paracrine ways. Importantly, senolytic treatment is effective

87 in mitigating musculoskeletal pathologies caused by *Chmp5* deletion.

88 **Results**

89 **Ablation of *Chmp5* in mouse osteogenic lineage cells causes aberrant**

90 **bone formation**

91 In addition to the well-characterized role of the CTSK gene in osteoclasts, this gene has
92 recently been reported to identify periskeletal progenitors [14-16]. In particular, the
93 ablation of *Chmp5* in mouse *Ctsk*-expressing cells (hereafter referred to as $Chmp5^{Ctsk}$
94 mice, homozygous) caused dramatic periskeletal bone overgrowth near the joint
95 compared to $Chmp5^{Ctsk/+}$ (heterozygous) and $Chmp5^{fl/fl}$ littermate controls (**Fig. 1A and**
96 **B**). Aberrant periskeletal bone growth in $Chmp5^{Ctsk}$ mice became distinct around
97 postnatal day 10 (d10), progressed with age, and involved multiple bones and joints
98 throughout the body, including knee, ankle, and foot joints (**Fig. 1A to C** and **Fig. S1A**).
99 With age, these animals developed severe skeletal deformities, progressive joint stiffness,
100 reduced motility, and short stature. Despite bone overgrowth in $Chmp5^{Ctsk}$ animals,
101 mechanical tests showed that bone stiffness and fracture stress decreased significantly
102 (**Fig. 1D**), suggesting that bone mechanical properties were impaired in $Chmp5^{Ctsk}$ mice.
103

104 To track $CTSK^+$ periskeletal progenitors during the bone overgrowth in $Chmp5^{Ctsk}$
105 mice, we crossed *Ctsk-Cre*, $Chmp5^{fl/fl}$, and $Rosa26^{mTmG}$ mice to generate
106 $Chmp5^{Ctsk/+};Rosa26^{mTmG/+}$ and $Chmp5^{Ctsk};Rosa26^{mTmG/+}$ reporter animals, in which
107 $CTSK^+$ periskeletal progenitors and their descendants express membrane-localized
108 green fluorescence protein (GFP). In $Chmp5^{Ctsk/+};Rosa26^{mTmG/+}$ control mice, GFP^+ cells
109 could be detected in the perichondrium, groove of Ranvier, periosteum, ligament, and
110 enthesis in addition to osteoclasts in the bone marrow, but not in growth plate

111 chondrocytes (**Fig. 1E**). With *Chmp5* deletion, GFP^{+} cells consisted of a major part of
112 cells in periskeletal overgrowth in *Chmp5^{Ctsk};Rosa26$^{mTmG/+}$* mice (**Fig. 1E** and **Fig. S1B**).
113 Tartarate resistant acid phosphatase (TRAP) staining did not show TRAP^{+} osteoclasts in
114 the periskeletal lesion, while obvious TRAP^{+} osteoclasts could be detected in the bone
115 marrow (**Fig. S1C**). These results indicate that *Chmp5*-deficient periskeletal progenitors
116 directly contribute to the bone overgrowth in *Chmp5^{Ctsk}* mice.
117
118 Next, we sought to confirm the role of CHMP5 in the regulation of bone formation by
119 deleting this gene using another mouse line of osteogenic lineage Cre. We crossed
120 *Chmp5$^{fl/fl}$* mice with the line of *Prrx1*-Cre [17], *Col2*-Cre [18] or *Osx*-Cre [19] mice to delete
121 the *Chmp5* gene in *Prrx1*-expressing limb mesenchymal progenitors (*Chmp5^{Prrx1}* mice),
122 *Col2*-expressing perichondral progenitors (*Chmp5^{Col2}* mice) or *Osx*-expressing
123 osteoprogenitors (*Chmp5^{Osx}* mice) and were unable to obtain postnatal homozygous
124 gene knockout mice, probably due to embryonic lethality after ablating C*hmp5* expression
125 in these osteogenic lineages. Subsequently, we used the *Dmp1*-Cre mouse line that could
126 target postnatal endosteal osteoprogenitors, preosteoblasts, mature osteoblasts, and
127 osteocytes [20-22]. *Chmp5^{Dmp1}* mice were born in normal Mendelian ratios and were
128 viable. Within three weeks of age, the skeletons of *Chmp5^{Dmp1}* mice began to show a
129 distinct expansion in comparison with *Chmp5$^{Dmp1/+}$* and *Chmp5$^{fl/fl}$* littermate controls,
130 which progressed with age and became much more severe at 1 year of age (**Fig. 1F**).
131 Bone expansion in *Chmp5^{Dmp1}* mice that occurred mainly in the endosteum was further
132 shown in detail around the age of 10 weeks by micro-CT and histological analyses (**Fig.
133 1G** and **Fig. S1D, E**).

134

135 Meanwhile, since *Dmp1*-expressing lineage cells also generate skeletal muscle cells
136 [21], *Chmp5*^{Dmp1} mice showed a profound decrease in skeletal muscle mass with age
137 (**Fig. 1F and H**). Hindlimb abduction, full-limb hanging time, and front-limb pull strength
138 tests showed that muscular functions also decreased profoundly in *Chmp5*^{Dmp1} compared
139 to *Chmp5*$^{fl/fl}$ mice (**Fig. 1I and J**).

140

141 CHMP5 restricts osteogenesis in skeletal progenitor cells

142 To further characterize the function of CHMP5 in the regulation of bone formation, we
143 cultured and sorted *Ctsk*-expressing periskeletal progenitor cells (CD45^{-};CD31^{-};GFP^{+})
144 from periskeletal tissues of *Chmp5*$^{Ctsk/+}$;*Rosa26*$^{mTmG/+}$ and *Chmp5*^{Ctsk};*Rosa26*$^{mTmG/+}$ mice
145 in the early stage of skeletal lesions (P10-P14) (**Fig. 2A and Fig. S2A, B**, hereafter
146 referred to as *Chmp5*$^{Ctsk/+}$ and *Chmp5*^{Ctsk} periskeletal progenitors, respectively). *Chmp5*
147 deletion in *Chmp5*^{Ctsk} periskeletal progenitors was confirmed by gene expression analysis
148 (**Fig. 2B**). Strikingly, when cultured in the osteogenic differentiation medium, *Chmp5*^{Ctsk}
149 periskeletal progenitors showed considerably enhanced osteogenesis in comparison with
150 *Chmp5*$^{Ctsk/+}$ control cells, as shown by alizarin red staining, von Kosaa staining, and
151 alkaline phosphatase activity assay (**Fig. 2C**).

152

153 The regulation of osteogenesis by CHMP5 in skeletal progenitors was further
154 determined in the osteogenic cell line MC3T3-E1 after removing *Chmp5* using
155 CRISPR/CAS9 technology (**Fig. 2D**). The deletion of *Chmp5* in MC3T3-E1 cells also
156 markedly increased osteogenesis, as shown by alizarin red staining at 2 weeks and 3

157 weeks of osteogenic induction (**Fig. 2E**). Consistently, the ingenuity pathway analysis of
158 RNA-seq data of *Chmp5*^{Ctsk} vs. *Chmp5*$^{Ctsk/+}$ periskeletal progenitors showed that multiple
159 molecular pathways related to osteoblast differentiation were activated with the *Chmp5*
160 deletion (**Fig. 2F**). Taken together, these results reveal a function of CHMP5 in regulating
161 osteogenesis in skeletal progenitors.
162

163 **CHMP5 controls skeletal progenitor cell senescence**

164 To gain more insight into the mechanism of regulation of bone formation by CHMP5, we
165 assumed that depletion of *Chmp5* in osteogenic lineage cells also increases cell
166 proliferation, which contributes to the bone overgrowth in *Chmp5* conditional knockout
167 mice. Unexpectedly, *Chmp5*^{Ctsk} periskeletal progenitors showed a significant decrease in
168 the cell proliferation rate compared to *Chmp5*$^{Ctsk/+}$ controls (approximately 58% decrease
169 in the cell number on day 6 of P2 culture, **Fig. 3A**). Because CHMP5 has been reported
170 to regulate thymocyte apoptosis [9], we performed cell apoptosis analyses for *Chmp5*^{Ctsk}
171 and *Chmp5*$^{Ctsk/+}$ cells. Annexin V staining showed that approximately 4.96 ± 0.81% of
172 *Chmp5*^{Ctsk} periskeletal progenitors vs. 1.69 ± 0.68% of *Chmp5*$^{Ctsk/+}$ control cells were
173 positively stained (**Fig. S3A**). Similarly, the in-situ terminal deoxynucleotidyl transferase
174 dUTP nick end labelling assay (TUNEL) demonstrated that around 3.70 ± 0.72% cells in
175 the periskeletal lesion of *Chmp5*^{Ctsk} mice were positively labelled (**Fig. S3B**). These
176 results show that cell apoptosis is activated in *Chmp5*^{Ctsk} periskeletal progenitors in a
177 rather low ratio.
178

179 Notably, the low apoptotic cell ratio (approximately 5%) could not well match the
180 decrease in cell proliferation rate (approximately 58%) in *Chmp5*^{Ctsk} periskeletal
181 progenitors. We further analyzed the RNA-seq data of *Chmp5*^{Ctsk} vs. *Chmp5*$^{Ctsk/+}$ cells to
182 dig out the mechanism of CHMP5 deficiency on the fate of skeletal progenitors. The gene
183 set enrichment analysis (GSEA) showed significant enrichment of genes in multiple
184 Reactome molecular pathways associated with cell senescence in *Chmp5*^{Ctsk} relative to
185 *Chmp5*$^{Ctsk/+}$ periskeletal progenitors, including *Hmga1*, *Hmga2*, *Trp53*, *Ets1*, and *Txn1*
186 (**Fig. 3B and C**). Meanwhile, GSEA of RNA-seq data also showed significant enrichment
187 of the SAUL_SEN_MAYO geneset (positively correlated with cell senescence) and the
188 KAMMINGA_SENESCENCE geneset (negatively correlated with cellular senescence) in
189 *Chmp5*^{Ctsk} vs. *Chmp5*$^{Ctsk/+}$ periskeletal progenitors (**Fig. S3C**).
190
191 Furthermore, Western blot results showed that both the p16 and p21 proteins, two
192 canonical markers of cellular senescence, were upregulated in *Chmp5*^{Ctsk} compared to
193 control cells, with a higher degree of upregulation in the p16 protein (**Fig. 3D**). However,
194 the mRNA levels of *Cdkn2a* (p16) and *Cdkn1a* (p21) did not show significant changes
195 according to the RNA-seq analysis (**Fig. S3D**). Furthermore, immunostaining for another
196 cell senescence marker γH2Ax demonstrated that there were significantly more
197 γH2Ax^{+};GFP^{+} cells in periskeletal overgrowth in *Chmp5*^{Ctsk};*Rosa26*$^{mTmG/+}$ mice relative to
198 the periosteum of *Chmp5*$^{Ctsk/+}$;*Rosa26*$^{mTmG/+}$ control mice (**Fig. 3E**). Accordingly,
199 C*hmp5*^{Ctsk} mice showed gross accelerated aging-related phenotypes, including hair loss,
200 joint stiffness/contracture, and decreased motility (**Fig. 3F**).
201

202 To further characterize the effect of CHMP5 on skeletal progenitor cell fate, we
203 deleted *Chmp5* in ATDC5 cells, which were shown to be an appropriate model of
204 periskeletal progenitors in a previous study [23], using CRISPR/CAS9 technology (**Fig.**
205 **S3E**). Similarly, *Chmp5* deletion also significantly suppressed the cell proliferation rate of
206 ATDC5 cells and mildly increased cell apoptosis (**Fig. S3F and G**). However, inhibition of
207 cell apoptosis using the pancaspase inhibitor Q-VD-Oph could not reverse cell number
208 reduction (**Fig. S3H**), indicating that cell apoptosis was not the main cause of the
209 decrease in the proliferation rate of *Chmp5*-deficient skeletal progenitors. Instead, cell
210 cycle analysis showed a significant decrease of *Chmp5*-deficient ATDC5 cells in phase
211 S, and a significant proportion of these cells were arrested in G0/G1 or G2/M phases (**Fig.**
212 **3G**), which is a typic characteristic of cell cycle arrest in senescent cells. Taken together,
213 these results at molecular, cellular, and gross levels demonstrate that *Chmp5* deficiency
214 induces skeletal progenitor cell senescence.
215

216 **Secretory phenotype of *Chmp5*-deficient skeletal progenitors**

217 A remarkable feature of senescent cells is the senescence associated secretory
218 phenotype (SASP), which plays a critical role in mediating the pathophysiological
219 processes of cell senescence [24]. In particular, periskeletal overgrowths in
220 *Chmp5*^{Ctsk};*Rosa26*$^{mTmG/+}$ mice showed evident integration of many cells lacking evidence
221 of Cre-mediated recombination (GFP^{-}) (**Fig. 1E**), suggesting that *Chmp5*-deleted
222 periskeletal progenitors might recruit neighboring *wild-type* cells to facilitate the bone
223 overgrowth. Additionally, the GSEA of RNA-seq data showed a significant enrichment of
224 genes associated with the SASP molecular pathway in *Chmp5*-deleted periskeletal

225 progenitors (**Fig. 4A**). Meanwhile, confocal fluorescence microscopy captured many
226 extracellular vesicles shed from the plasma membrane of *Chmp5*^{Ctsk} periskeletal
227 progenitors, which were rarely detected around *wild-type* control cells (**Fig. 4B**).
228 Furthermore, nanoparticle tracking analysis demonstrated higher concentrations of
229 extracellular vesicles in the culture medium of *Chmp5*^{Ctsk} periskeletal progenitors
230 compared to *wild-type* control cells (**Fig. 4C, D** and **Fig. S4A**). These results show that
231 *Chmp5* deficiency activates the SASP molecular pathway and increases the secretion of
232 skeletal progenitors.
233
234 Functionally, conditioned medium collected from *Chmp5*-deficient skeletal
235 progenitors caused a higher proliferation rate of ATDC5 cells than medium from control
236 cells (**Fig. 4E**). Meanwhile, coculture of *wild-type* with *Chmp5*^{Ctsk} periskeletal progenitors
237 promoted osteogenesis of *wild-type* cells (**Fig. S4B**). Simultaneously, CD45^{-};CD31^{-};GFP^{-}
238 skeletal progenitors from periskeletal tissues of *Chmp5*^{Ctsk};*Rosa26*$^{mTmG/+}$ mice showed
239 increased proliferation along with enhanced osteogenic differentiation compared to the
240 corresponding cells from *Ctsk-Cre;Rosa26*$^{mTmG/+}$ control mice (**Fig. 4F, G** and **Fig. S4C,**
241 **D**). Immunostaining for the cell proliferation marker Ki-67 demonstrated an increase in
242 the number of stained cells in the periskeletal lesion of *Chmp5*^{Ctsk} mice (**Fig. S4E**). Since
243 GFP^{+} *Chmp5*^{Ctsk} periskeletal progenitors showed a decreased cell proliferation rate and
244 increased cell senescence (**Fig. 3**), and the GFP^{-} *Chmp5*^{Ctsk} periskeletal progenitors
245 showed an increased cell proliferation rate (**Fig. 4F** and **Fig. S4C**), these Ki-67^{+} cells in
246 **Fig. S4E** should represent GFP^{-} skeletal progenitors in the periskeletal lesion. Together,

247 these results demonstrate that *Chmp5*-deficient skeletal progenitors could promote the
248 proliferation and osteogenesis of surrounding *wild-type* skeletal progenitors.
249
250 Next, we performed a secretome analysis to characterize secretory profiles of
251 *Chmp5*^{Ctsk} vs. *wild-type* periskeletal progenitors. Fifteen proteins were found to increase
252 and five proteins to decrease in the cell supernatant of *Chmp5*^{Ctsk} periskeletal progenitors
253 (**Fig. 4H** and **Fig. S4F**). In particular, all 15 upregulated proteins, including NCAM1,
254 CSPG4, SDF4, NME2, TAGLN, OLFML2B, PXDN, COL4A1, FSTL1, TPI1, MFGE8,
255 COL1A2, COL1A1, HSPG2, and COL3A1, have been identified in the osteoblastic cell
256 secretome or in the regulation of osteoblast differentiation or functions [25, 26]. Western
257 blot verified upregulation of two of these proteins, COL1A1 and TAGLN, in the cell
258 supernatant of *Chmp5*^{Ctsk} vs. *wild-type* periskeletal progenitors (**Fig. 4I**). Notably, the
259 secretome analysis did not detect common SASP factors, such as cytokines and
260 chemokines, in the secretory profile of *Chmp5*^{Ctsk} periskeletal progenitors, probably due
261 to their small molecular weights and the technical limitations of the mass-spec analysis.
262 Taken together, these results demonstrate a secretory phenotype and paracrine actions
263 of *Chmp5*-deficient skeletal progenitors. However, factors that mediate the paracrine
264 actions of *Chmp5*-deficient periskeletal progenitors remain further clarified in future
265 studies.
266

267 Senolytic treatment mitigates musculoskeletal pathologies in *Chmp5*
268 conditional knockout mice

269 To affirm the role of cell senescence of osteogenic cells in contributing to bone overgrowth
270 in *Chmp5*^{Ctsk} and *Chmp5*^{Dmp1} mice, we treated *Chmp5*-dificient periskeletal progenitors
271 and animals with the senolytic drugs quercetin and dasatinib (Q + D), which have been
272 widely used to eliminate senescent cells under various physiological and pathological
273 conditions [27, 28], and assessed the therapeutic efficacy. First, in vitro Q + D treatment
274 showed that *Chmp5*^{Ctsk} periskeletal progenitors were more sensitive to senolytic drugs
275 for cell apoptosis compared to control cells (**Fig. 5A**). *Chmp5*^{Ctsk} animals were then
276 treated with Q + D from the first two weeks after birth for 7 weeks and showed a
277 significantly improved periskeletal bone overgrowth and animal motility compared to
278 *Chmp5*$^{fl/fl}$ control animals (**Fig. 5B** and **Fig. S5**). Similarly, treatment of *Chmp5*^{Dmp1} mice
279 with Q + D also improved musculoskeletal manifestations, including hindlimb abduction,
280 the whole femur and cortical bone thickness, and partially restored skeletal muscle
281 functions (**Fig. 5C-E**). An improvement in animal motility was also found with Q + D
282 treatment in adult mice. There were no apparent abnormalities in *Chmp5*$^{fl/fl}$ control
283 animals treated with the same dose of Q + D in parallel.
284
285 Furthermore, to verify the efficacy of senolytic drugs in treating the periskeletal bone
286 overgrowth in *Chmp5*^{Ctsk} mice, we used another senolytic drug Navitoclax (ABT-263),
287 which is a BCL-2 family inhibitor and specifically induces apoptosis of senescent cells [29,
288 30]. Micro-CT analysis demonstrated that ABT-263 could also relieve periskeletal bone
289 overgrowth in *Chmp5*^{Ctsk} mice (**Fig. 5F**). Together, these results demonstrate that the
290 elimination of senescent cells using senolytic drugs is effective in alleviating
291 musculoskeletal pathologies in *Chmp5*^{Ctsk} and *Chmp5*^{Dmp1} animals, confirming that

292 osteogenic cell senescence is responsible for musculoskeletal abnormalities in *Chmp5*^{Ctsk}
293 and *Chmp5*^{Dmp1} mice.
294

295 **CHMP5 is essential for endolysosomal functions and maintaining**
296 **VPS4A protein in skeletal progenitors**

297 Next, we wondered whether *Chmp5* deficiency in skeletal progenitors affects the
298 endocytic pathway. Notably, approximately 45% of *Chmp5*^{Ctsk} periskeletal progenitors
299 contained enlarged GFP^{+} vesicles, which were rarely found in *wild-type Ctsk*$^{+}$ periskeletal
300 progenitors (**Fig. 6A**), suggesting a possible issue of the endocytic pathway in *Chmp5*-
301 deleted skeletal progenitors. Next, we used molecular markers for different components
302 and the function of the endocytic pathway to elucidate the influence of *Chmp5* deficiency
303 on the endolysosomal system in skeletal progenitors (**Fig. 6B**).
304

305 The LysoTracker Red DND-99 trace and the immunostaining of lysosome-
306 associated membrane protein 1 (LAMP1) showed positive staining in many of the
307 enlarged vesicles in *Chmp5*^{Ctsk} periskeletal progenitors (**Fig. 6C** and **Fig. S6A, B**). The
308 quantification of the number and average size of LAMP1 stained vesicles were further
309 performed in ATDC5 cells with or without *Chmp5* deletion (**Fig. 6D**). Next, the number
310 and size of the vesicles stained for the late endosome marker RAB7 also increased
311 markedly in *Chmp5*-deficient relative to *wild-type* skeletal progenitors (**Fig. 6E, F**).
312 Meanwhile, many of these accumulated vesicles were double positive for LAMP1 and
313 RAB7 (**Fig. S6C, D**), suggesting that they are terminal compartments in the endocytic
314 pathway. Accordingly, the transmission electron microscopy demonstrated a significant

315 accumulation of MVB-like and lysosome-like structures with different electronic density in
316 *Chmp5*^{Ctsk} periskeletal progenitors (**Fig. 6G**).
317
318 To examine the function of the endocytic pathway, we used a pH-sensitive
319 fluorescent EGF conjugate and traced the degradation of the internalized EGF receptor
320 in *Chmp5*^{Ctsk} vs. *wild-type* periskeletal progenitors. *Chmp5* deficiency significantly
321 delayed the degradation of the EGF conjugate in *Chmp5*^{Ctsk} periskeletal progenitors (**Fig.**
322 **6H**), indicating altered function of the endocytic pathway. It should be noted that the early
323 endosomes of EEA1^{+} also increased slightly in approximately 10% of *Chmp5*^{Ctsk}
324 periskeletal progenitors, while the recycling endosomes of RAB11^{+} and the TGN38^{+} trans-
325 Golgi network were relatively normal (**Fig. S6E**). These results demonstrate that CHMP5
326 deficiency in skeletal progenitors causes the accumulation of late endosomes and
327 lysosomes and disrupts the function of the endolysosomal pathway.
328
329 To dissect the molecular mechanism of CHMP5 that regulates the endolysosomal
330 pathway, we performed a proteomic analysis in *Chmp5*^{Ctsk} and *wild-type* periskeletal
331 progenitors. Bioinformatic analyses of proteomic data showed that VPS4A is one of the
332 most significant decreased proteins in *Chmp5*^{Ctsk} compared to *wild-type* periskeletal
333 progenitors (**Fig. 6I**). The decrease in the VPS4A protein in *Chmp5*^{Ctsk} periskeletal
334 progenitors was verified by Western blot analysis (**Fig. 6J**), while the *Vps4a* mRNA did
335 not show a significant change in the RNA-seq analysis (**Fig. S6F**). On the other hand,
336 when CHMP5 was overexpressed by transfection of a CHMP5 vector into HEK-293T cells,
337 the level of VPS4A protein increased significantly and *VPS4A* mRNA was not significantly

338 affected (**Fig. S6G, H**). These results indicate that CHMP5 is essential in maintaining the
339 VPS4A protein. Since VPS4A is a critical ATPase mediating the function of the ESCRT-
340 III protein complex, the reduction of VPS4A protein could be responsible for
341 endolysosomal dysfunction in *Chmp5*-deleted skeletal progenitors.
342

343 Mitochondrial dysfunction is responsible for cell senescence in 344 *Chmp5*-deleted skeletal progenitors

345 A remaining question is how *Chmp5* deficiency and endolysosomal dysfunction cause
346 skeletal cell senescence. Impairment of lysosomal functions could hinder the degradation
347 of damaged mitochondria, resulting in the accumulation of reactive oxygen species (ROS)
348 in mitochondria [31, 32]. Indeed, the GSEA of RNA-seq data showed significant
349 enrichment of genes associated with the molecular pathway of oxidative stress-induced
350 cell senescence in *Chmp5*^{Ctsk} vs. *Chmp5*$^{Ctsk/+}$ periskeletal progenitors (**Fig. 7A**).
351 Accordingly, the level of mitochondrial ROS and the abundance of mitochondria
352 increased markedly in *Chmp5*-deficient compared to *wild-type* skeletal progenitors, as
353 shown by CellRox, tetramethylrhodamine methyl ester (TMRE), and MitoTracker
354 fluorescence stain, and expression levels of mitochondrial inner membrane proteins
355 NDUF88, SDHB, and ATP5A (**Fig. 7B to D** and **Fig. S7A, B**).
356

357 Mitochondrial functions were also compromised in *Chmp5*-deficient skeletal
358 progenitors as shown by decreased mitochondrial respiratory capacity, increased
359 extracellular acidification rate, and reduced tolerance to galactose (**Fig. 7E and F**).
360 Furthermore, mitochondrial dysfunction and DNA damage response usually form a

361 feedback loop to drive senescent cell phenotypes [33-35]. The GSEA of the RNA-seq
362 data also showed enrichment of genes associated with DNA damage-induced cell
363 senescence in *Chmp5*^{Ctsk} vs. *Chmp5*$^{Ctsk/+}$ skeletal progenitors (**Fig. S7C**). Upregulation
364 of two critical DNA damage-responsive genes *H2afx* and *Trp53* was verified by qPCR in
365 *Chmp5*^{Ctsk} relative to *Chmp5*$^{Ctsk/+}$ skeletal progenitors (**Fig. S7D**). Importantly, N-
366 Acetylcysteine (NAC) antioxidant treatment could reverse the reduced activity of cell
367 proliferation in *Chmp5*-deficient skeletal progenitors (**Fig. 7G**). Therefore, the
368 accumulation of dysfunctional mitochondria and mitochondrial ROS is responsible for cell
369 senescence in *Chmp5*-deficient skeletal progenitors.

370 ## Discussion

371 In this study, our results reveal the role and mechanism of CHMP5 in the regulation of
372 cell senescence and bone formation in osteogenic cells. In normal skeletal progenitor
373 cells, CHMP5 is essential in maintaining the VPS4A protein, a critical AAA ATPase for
374 the functions of the ESCRT-III protein complex. The deficiency of CHMP5 decreases the
375 VSP4A protein and causes the accumulation of dysfunctional late endosomes (MVB),
376 lysosomes, and mitochondria, which induce skeletal cell senescence and result in
377 increased bone formation through a combination of cell-autonomous and paracrine
378 mechanisms (**Fig. 7H**). Strikingly, elimination of senescent cells using senolytic drugs is
379 effective in mitigating abnormal bone formation.

380

381 The role of CHMP5 in cell senescence has not been reported. As the mechanisms
382 and functions of cell senescence could be highly heterogeneous depending on inducers,
383 tissue and cell contexts, and other factors such as “time” [36-38], there is currently no
384 universal molecular marker to define all types of cell senescence. In this study, *Chmp5*-
385 deficient skeletal progenitors show multiple canonical features of senescent cells,
386 including increased p16 and p21 proteins and γH2Ax^{+} cells, cell cycle arrest, elevated
387 secretory phenotype, accumulation and dysfunction of lysosomes and mitochondria. Also,
388 *Chmp5*^{Ctsk} and *Chmp5*^{Dmp1} mice show dramatic aging-related phenotypes, including hair
389 loss, joint stiffness/contracture, decreased bone strength, or gradual loss of muscle mass
390 and functions. Importantly, senolytic drugs markedly improve musculoskeletal
391 abnormalities and increase animal motility in *Chmp5*^{Ctsk} and *Chmp5*^{Dmp1} mice. These
392 results reveal the role of CHMP5 in controlling the senescence of skeletal cells.

393 CHMP5 has been reported to regulate VPS4 activity, which catalyzes the
394 disassembly of the ESCRT-III protein complex from late endosomes/MVBs, by binding
395 directly to the VPS4 protein or other protein partners such as LIP5 and Brox [39, 40].
396 However, it remains unknown how CHMP5 regulates VPS4 activity. Our results in this
397 study show that CHMP5 is necessary to maintain the VPS4A protein but does not affect
398 the level of VPS4A mRNA, suggesting that CHMP5 regulates VPS4 activity by
399 maintaining the level of the VPS4A protein. However, the mechanism of CHMP5 in the
400 regulation of the VPS4A protein has not yet been studied. Since CHMP5 can recruit the
401 deubiquitinating enzyme USP15 to stabilize IκBα in osteoclasts by suppressing
402 ubiquitination-mediated proteasomal degradation [8], it is also possible that CHMP5
403 stabilizes the VPS4A protein by recruiting deubiquitinating enzymes and regulating the
404 ubiquitination of VPS4A, which needs to be clarified in future studies. Notably, mutations
405 in the *VPS4A* gene in humans can cause multisystemic diseases, including
406 musculoskeletal abnormalities [41] (OMIM: 619273), suggesting that normal expression
407 and function of VPS4A are important for musculoskeletal physiology. The roles of VPS4A
408 in regulating musculoskeletal biology and cell senescence should be further explored in
409 future studies.
410
411 The upstream signaling that regulates CHMP5 expression in osteogenic cells is
412 unclear. Previous studies showed that muramyl-dipeptide and lipopolysaccharide
413 upregulate CHMP5 expression in human monocytes [42, 43]. Whether the mechanism
414 also occurs in osteogenic cells remains to be determined, especially since many
415 molecular and cellular mechanisms are cell lineage/type dependent. In addition, an earlier

416 study showed that *Rank* haploinsufficiency in *Chmp5*^{Ctsk} mice (*Chmp5*^{Ctsk}*;Rank*$^{+/-}$) could
417 greatly reverse skeletal abnormalities in these animals, including periskeletal overgrowth
418 [8]. Therefore, RANK receptor signaling may function upstream of CHMP5. However,
419 whether RANK is expressed in osteogenic cells needs additional studies to clarify.
420 Otherwise, other epigenetic, transcriptional, translational, or post-translational
421 mechanisms may also play a role in the regulation of CHMP5 expression in osteogenic
422 lineage cells in physiological and pathological contexts.
423
424 A previous study using the *Chmp5*^{Ctsk} mouse model defined a function of CHMP5
425 in the regulation of osteoclast differentiation by tuning NF-κB signaling [8]. While the
426 evidence on the role of CHMP5 in osteoclastogenesis is robust in that study, our results
427 in the current study provide compelling evidence on the role of CHMP5 in bone formation
428 in osteogenic cells. Furthermore, the function of CHMP5 in restricting bone formation was
429 confirmed in the *Chmp5*^{Dmp1} mouse model and in the MC3T3-E1 cell model (Figs. 1 and
430 2). Therefore, it is probable that both osteoclast and osteoblast lineage cells contribute to
431 bone deformation in *Chmp5*^{Ctsk} mice. However, the previous study by Greenblatt et al.
432 did not find endolysosomal abnormalities in osteoclasts after *Chmp5* deletion, and in that
433 study cell senescence and mitochondrial functions were not measured. Also, a previous
434 study by Adoro et al. did not detect endolysosomal abnormalities in *Chmp5*-deficient
435 developmental T cells [9]. Since both osteoclasts and T cells are of hematopoietic origin,
436 and meanwhile osteogenic cells and MEFs, which show endolysosomal abnormalities
437 after CHMP5 deficiency, are of mesenchymal origin, it turns out that the function of

438 CHMP5 in regulating the endolysosomal pathway could be cell lineage-specific, which
439 remains clarified in future studies.
440
441 Furthermore, it is unclear whether the effect of senolytic drugs in *Chmp5*^{Ctsk} mice
442 involves targeting osteoclasts other than osteogenic cells, as osteoclast senescence has
443 not yet been evaluated. However, the efficacy of Q + D in targeting osteogenic cells,
444 which is the focus of the current study, was confirmed in *Chmp5*^{Dmp1} mice (Fig. 5C-E).
445 Additionally, Q + D caused a higher cell apoptotic ratio in *Chmp5*^{Ctsk} compared to *wild-*
446 *type* periskeletal progenitors in *ex vivo* culture (Fig. 5A), demonstrating the effectiveness
447 of Q + D in targeting osteogenic cells in the *Chmp5*^{Ctsk} model. Furthermore, an alternative
448 senolytic drug ABT-263 could also ameliorate periskeletal bone overgrowth in *Chmp5*^{Ctsk}
449 mice (Fig. 5F). Together, these results confirm that osteogenic cell senescence is
450 responsible for the bone overgrowth in *Chmp5*^{Ctsk} and *Chmp5*^{Dmp1} mice and senolytic
451 treatments are effective in alleviating these skeletal disorders.
452
453 Notably, aging is associated with decreased osteogenic capacity in marrow stromal
454 cells, which is related to conditions with low bone mass, such as osteoporosis. Rather,
455 aging is also accompanied by increased ossification or mineralization in musculoskeletal
456 soft tissues, such as tendons and ligaments [44]. In particular, the abnormal periskeletal
457 overgrowth in *Chmp5*^{Ctsk} mice was predominantly mapped to the insertion sites of
458 tendons and ligaments on the bone (Fig. 1A and E), which is consistent with changes
459 during aging and suggests that mechanical stress at these sites could contribute to the
460 aberrant bone growth. These results suggest that skeletal stem/progenitor cells at

461 different sites of musculoskeletal tissues could demonstrate different, even opposite
462 outcomes in osteogenesis, due to cell senescence.
463
464 In addition, there was also a mild increase in apoptotic cells in the population of
465 *Chmp5*-deficient skeletal progenitors (approximately 5%). Since anti-apoptotic treatment
466 with the pan-caspase inhibitor Q-VD-Oph could not reverse the decrease in cell number
467 in *Chmp5*-deficient skeletal progenitors, cell apoptosis may not be the main cause of the
468 decrease in cell proliferation rate in these progenitors. It should be noted that although
469 senescent cells are generally resistant to apoptosis, the gradual accumulation of
470 dysfunctional lysosomes and mitochondria in *Chmp5*-deficient skeletal progenitors could
471 result in overload of toxic macromolecules and metabolites, which could activate the
472 apoptotic pathway to eliminate severely damaged cells. Otherwise, CHMP5 may regulate
473 cell senescence and apoptosis through different mechanisms.
474
475 In summary, we have revealed the role of CHMP5 in the regulation of cell
476 senescence and bone formation in osteogenic cells. This study also confirms the
477 essential function of CHMP5 in the endolysosomal pathway that involves the regulation
478 of the VPS4A protein. Additionally, mitochondrial functions are impaired with CHMP5
479 deletion, which is responsible for cell senescence. Future studies should explore the
480 mechanism of CHMP5 in the regulation of mitochondrial functions. Since $Chmp5^{Ctsk}$ and
481 $Chmp5^{Dmp1}$ mice recapitulate many cellular and phenotypic features of musculoskeletal
482 lesions in lysosomal storage disease, these animals could be used as preclinical models
483 to investigate the mechanism and test therapeutic drugs for these intractable disorders.

Acknowledgments

We thank Dr. Sankar Ghosh for providing *Chmp5*-floxed mice; Drs. Gregory Hendricks and Lara Strittmatter at the University of Massachusetts Chan Medical School for help in interpreting TEM data; Dr. Tomer Shpilka for assistance in running the Seahorse analyzer; Drs. Guangchuang Yu and Jiyeon Park for independently analyzing the RNA-seq data. Dr. Chunjing Bian for generating the CHMP5 overexpression vector. X.G. is supported by the National Natural Science Foundation of China (project 2-2-008-0213) and the Beijing Natural Science Foundation (project 5222008). J.H.S. holds support from the NIH (R21AR077557, R01AR078230) and AAVAA Therapeutics.

Contributions

X.G. perceived the project, designed experiments, interpreted the results, and wrote and reviewed the manuscript; F.Z., Y.W., L.Z., C.W. and X.G. performed experiments and analyzed the results; D.C. and R.X. provided critical resources for the study; H.L. contributed to part of RNA-seq data analyses; C.M.H. offered suggestions and main reagents for mitochondrial analyses; J.H.S. partly supported the study and reviewed the manuscript.

Competing interests

The study started when the corresponding author (X. Ge) worked at the University of Massachusetts Medical School and a previous manuscript related to this study was posted on bioRxiv (https://doi.org/10.1101/2020.08.03.233874). To complete the study for a peer-reviewed publication, the co-first authors and X. Ge generated a novel *Chmp5*-

507 floxed mouse strain, re-established all animal and cell models in the current laboratory in
508 Beijing, China, and added novel critical experiments to make the conclusion convincing
509 and the study comprehensive. Therefore, we reorganized the data and wrote it as a new
510 paper. All authors agree on the current version of the paper, including its authorship and
511 conclusions. J.H.S. is a scientific co-founder of AAVAA Therapeutics and holds equity in
512 this company but does not have conflicts of interest with this study. Other authors declare
513 no competing interests.

514 # Methods

515 ## Mice

516 In this study, two *Chmp5*-flox mouse strains were used, and similar phenotypes were
517 observed. The *Chmp5*$^{tm2.1Gho}$ strain was previously described [8]. The alternative *Chmp5*-
518 flox strain was established by CRISPR/Cas9-mediated genome engineering. Similarly to
519 the *Chmp5*$^{tm2.1Gho}$ strain, exons 4 and 5 were selected as the conditional knockout region
520 in the newly created strain and deletion of this region results in frameshift of the *Chmp5*
521 gene. To engineer the target vector, homologous arms, and the conditional knockout
522 region with 5' and 3' loxP sites were generated by PCR using the BAC clone. Cas9, gRNA,
523 and targeting vectors were co-injected into fertilized eggs for gene-edited mouse
524 production and pups were genotyped by PCR followed by sequencing analysis. Mice
525 bearing the targeted allele were backcrossed with C57BL/6J mice up to F8 generation.
526

527 Ctsk$^{tm1(cre)Ska}$ (Ctsk^{Cre}), B6N.FVB-Tg(Dmp1-cre)1Jqfe/BwdJ (Dmp1-Cre), B6.Cg-
528 Tg(Prrx1-cre)1Cjt/J (Prrx1^{Cre}), B6;SJL-Tg(Col2a1-cre)1Bhr/J (Col2-Cre), and B6.Cg-
529 Tg(Sp7-tTA,tetO-EGFP/cre)1Amc/J (Osx1-GFP::Cre) mice have previously been
530 reported [8, 17, 45-47]. While the Ctsk-Cre strain is a knockin mouse line, other strains
531 (Dmp1-Cre, Prrx1-Cre, Col2-Cre, and Osx-Cre) are transgenic lines. The
532 Gt(ROSA)26Sor$^{tm4(ACTB-tdTomato,-EGFP)Luo}$ (Rosa26^{mTmG}) mice were purchased from Jackson
533 Laboratories. To generate experimental animals, *Chmp5*$^{fl/fl}$ mice were crossed with
534 *Chmp5*$^{Ctks/+}$ and *Chmp5*$^{Dmp1/+}$ mice, respectively. To generate reporter mouse lines,
535 *Chmp5*$^{Ctks/+}$ mice were mated with *Chmp5*$^{fl/fl}$;*Rosa26*^{mTmG} mice, and Ctsk^{Cre} mice were
536 crossed with Rosa26^{mTmG} animals.

537

538 All mice were kept in C57BL/6J background and housed in the standard animal
539 facility on a 12-hour light/dark cycle with ad libitum access to water and standard chow.
540 In most situations, the littermates were compared otherwise as indicated. All animals
541 were used in accordance with the Guide for Care and Use of Laboratory Animals (NIH,
542 United States) and were handled according to protocols approved by IACUC at the
543 University of Massachusetts Medical School (Worcester, United States) and Capital
544 Medical University (Beijing, China). The biological and technical replicates (*n* numbers)
545 for each animal experiment are reported in the figure legends. In this study, both sexes
546 of mice were used and, unless otherwise stated, no gender differences were observed in
547 the reported phenotypes.

548

549 **Micro-CT and radiography**

550 Micro-CT analyses were performed using the Scanco μCT-35 or μCT-40 scanner
551 (Scanco Medical). Images were processed using the Inveon Research Workplace
552 (Siemens Medical Solutions). X-ray images were acquired using the X-Ray MX-20
553 Specimen (Faxitron) following the default programme.

554

555 **Histology, immunohistochemistry, and immunofluorescence**

556 All samples were fixed in 10% neutral formalin or 4% paraformaldehyde overnight for
557 premature samples or 2 days for mature skeletal samples. Samples were decalcified
558 with 14% EDTA and serial sections were cut for all samples. At least five slides were
559 selected at a certain interval (80-100 μm) from each sample for histological evaluation.

560 Fate-mapping images were acquired using a Leica TCS SP5 II laser scanning confocal
561 microscope.
562
563 Immunofluorescence for γH2AX was performed using a Phospho-Histone H2A.X
564 (Ser139) antibody (clone 20E3, CST). Immunohistochemistry for Ki-67 was performed
565 using the VECTASTAIN® Elite® ABC HRP Kit (Peroxidase, Rabbit IgG; Vector
566 Laboratories). Cells for immunofluorescence were cultured in 35 mm MatTek glass
567 bottom dishes (No. 1.5 coverslip, MatTek Corporation). Briefly, tissues or cells were
568 fixed in 4% PFA for 15 min, blocked in 1% BSA for 30 min, and incubated with primary
569 antibodies for 2 hrs and then fluorescence conjugated secondary antibodies for 1 hr.
570 Images were acquired using the Leica TCS SP5 II laser scanning confocal microscope.
571 The quantification of intracellular vesicles was performed using FIJI software following
572 the particle analysis procedure (https://imagej.net/imagej-wiki-static/Particle_Analysis,
573 NIH).
574
575 **Bone mechanical test**
576 The femurs of *Chmp5*^{Ctsk} and *Chmp5*$^{fl/fl}$ mice at 6-7 weeks of age were subjected to
577 mechanical testing using the DMA Q800 mechanical test system with the 3-point
578 bending mode following the manufacturer's procedure (TA Instruments, USA). The
579 femurs were placed in a direction of the anterior surface downward and the posterior
580 aspect of the femoral condyles facing upward. The span length (L) was 10 mm and the
581 load was applied in the middle of the bone. Five mice per group were used and bone

582 stiffness and ultimate stress (fracture stress) from male mice were reported. Similar
583 changes were observed in both sexes.
584
585 **Tests of skeletal muscle functions**
586 The four-limb hanging test was performed using the top grid of a mouse cage [48]. The
587 grid was set at a height of about 35 cm, and the measurement was repeated for 3-5
588 times for each mouse at a rest interval of about 3-5 min. The maximum hang time was
589 recorded for each animal. Both male and female animals were included in this
590 experiment, and there was no significant sex difference regarding the four-limb hanging
591 time.
592
593 The forelimb grip strength test was carried out using an electronic scale as
594 described with slight modification [48, 49]. A mouse was allowed to grasp the gauze
595 attached on the scale. The scale was reset to 0 g after stabilization and a researcher
596 slowly pulled the mouse's tail backward. Five consecutive measurements were
597 performed for each mouse and the peak pull force in grams was recorded. A significant
598 sex difference was observed in the forelimb grip strength. Both male and female mice
599 were included in this study and the same trend of changes was found in both genders.
600
601 **Skeletal progenitor cell culture and sorting**
602 The periskeletal progenitors were isolated from the hindlimbs of *Ctsk-*
603 *Cre;Rosa26*$^{mTmG/+}$, *Chmp5*$^{Ctsk/+}$*;Rosa26*$^{mTmG/+}$, and *Chmp5*^{Ctsk}*;Rosa26*$^{mTmG/+}$ mice (*n* =
604 10 animals per genotype) at 2 weeks of age according to the previously established

605 method [23]. Briefly, the periskeletal tissues were dissected, minced into small pieces,
606 and digested with 1 mg/ml collagenase type I (Worthington), 1 mg/ml collagenase type
607 II (Worthington) and 1.5 mg/ml dispase (Roche) for 30 min at 37°C. Cells were cultured
608 in skeletal stem cell medium (Joint Therapeutics, Beijing, China) for one week, stained
609 with anti-CD31 and anti-CD45 antibodies, and sorted using a FACSAria II cell sorter
610 (BD Biosciences) for further analyses.
611
612 In all experiments, *Chmp5*^{Ctsk} and control cells from littermate mice were cultured,
613 sorted, and re-seeded in parallel for subsequent analyses. The coculture experiment was
614 carried out by directly mixing 90% *wild-type* skeletal progenitors with 10% *Chmp5*^{Ctsk}
615 or control periskeletal progenitors to simulate the in vivo context of cell-cell contact in
616 periskeletal overgrowth. The cocultures were induced in osteogenic differentiation
617 medium for 4 weeks. The biological and technical replicates (*n*-numbers) for each cellular
618 experiment are reported in the figure legends.
619
620 **CRISPR/CAS9 lentiviral infection**
621 Pairs of CRISPR guide RNA oligos (mouse *Chmp5* single guide RNAs [sgRNAs] targeting
622 GGCTCCGCCACCTAGCTTGA and GTTTCGCTTTTCCGAAGAAT on exon 1
623 respectively) were annealed and cloned into the BsmBI sites of the lentiCRISPR V2-puro
624 vector (plasmid 52961, Addgene). CRISPR lentiviral plasmids and lentiviral packaging
625 plasmids (pMDLg/pRRE, pRSV-Rev, and pMD2.G; Addgene) were transfected into HEK
626 293T cells. The supernatants were harvested and filtered through a 0.45-μm filter 2.5
627 days after transfection. MC3T3-E1 and ATDC5 cells were infected with CRISPR lentivirus

628 and selected with puromycin (4.5 μg/ml, Clontech) for 7 days. The depletion of *Chmp5*
629 was confirmed by Western blotting.
630
631 ***In vitro* osteogenesis**
632 For osteogenic differentiation, 1.0 x 10^5 cells were seeded in each well of 24-well plates
633 and cultured overnight. Cells were changed into osteogenic media (Joint Therapeutics)
634 the next day and induced for the indicated times. Osteogenesis was determined by
635 alizarin red and von Kossa staining and by examining the activity of alkaline
636 phosphatase.
637
638 **Cell cycle, proliferation, and apoptosis analyses**.
639 The cell number was counted with a Countess II FL Automated Cell Counter
640 (ThermoFisher Scientific, USA) at indicated time intervals. The AlamarBlue cell viability
641 assay was performed as previously described [23]. The cell cycle was determined using
642 the APC-BrdU Flow Kit (BD Biosciences). In vitro apoptosis analysis was carried out
643 with Annexin V-PI staining and in situ cell apoptosis was determined with TUNEL
644 staining (Abcam).
645
646 **RNA-seq, data analysis, and functional annotation**
647 The sorted *Chmp5*^{Ctsk} and *Chmp5*$^{Ctsk/+}$ periskeletal progenitors were subjected to RNA-
648 seq For library preparation, 100 ng of total RNA from each sample was subjected to rRNA
649 depletion with the NEBNext rRNA Depletion Kit (New England Biolabs) according to the
650 manufacturer's manual. Subsequently, the rRNA-depleted RNA was used to build the

651 RNA-seq library with the NEBNext Ultra II Directional RNA Library Prep Kit (New England
652 Biolabs) according to the manufacturer's manual. The index of each RNA-seq library was
653 introduced using NEBNext Multiplex Oligos for Illumina (New England Biolabs). Each
654 RNA-seq library was analyzed by the fragment analyzer (Advanced Analytical
655 Technologies) and quantified by the KAPA Library Quantification Kit (KAPA Biosystems)
656 according to the manufacturer's manual. An equal amount of each RNA-seq library was
657 mixed for sequencing in one lane of Illumnia HiSeq3000 in paired-end 150 base mode
658 (Illumina).
659
660 The raw Illumina pair-end reads were first aligned with ribosomal RNA (GenBank ID
661 BK000964.1) with Bowtie2 v2.2.6 [50]. Reads that failed to map to ribosomal RNA were
662 aligned with the mouse reference genome mm10 with STAR v2.5.3 [51]. Differential
663 analysis was performed with Cuffdiff v2.2.1 [52]. The raw data were analyzed by two
664 independent statisticians and similar results were obtained.
665
666 Pathway analyses were performed for differentially expressed genes using the
667 Reactome online analysis tool [53] and the Ingenuity Pathway Analysis software (Qiagen).
668 Gene ontology term over-representation analysis was run using PANTHER (version 14.1)
669 with all genes expressed in a tissue or cell type as background and the differentially
670 expressed gene list as input. The P-values of Fisher's exact tests were corrected by
671 controlling the false discovery rate (FDR). Gene set enrichment analyses were performed
672 using GSEA or ConsensusPathDB. For GSEA-based analysis, gene sets of interests

673 were downloaded from the MsigDB, while all built-in gene sets were used for
674 ConsensusPathDB-based analysis.
675
676 **Nano LC-MS/MS for secretomic and proteomic analyses**
677 Label-free relative protein quantification analyses were performed to identify differentially
678 expressed proteins in the supernatant or cell lysis of *Chmp5*^{Ctsk} versus control periskeletal
679 progenitors (*n* =3 animals per group). For cell supernatants, the same amounts of
680 samples went through 3 kD ultrafiltration tubes and then were processed for reduction
681 and alkylation. Subsequently, the samples were digested in trypsin overnight and the
682 peptides were desalted prior to mass spectrometry analysis. For cell lysis, samples were
683 precipitated using acetone after reduction and alkylation. The samples were then
684 subjected to digestion, desalination, and mass spectrometry analysis.
685
686 Quantitative data were collected on an Orbitrap Eclipse™ Tribrid™ mass spectrometer
687 (ThermoFisher Scientific) coupled to a nanoLC system (EASY-nLC™ 1200,
688 ThermoFisher Scientific). All peptide mixtures were analyzed using the same
689 chromatographic conditions: 5 µl of each sample were fractionated in a 150 µm×15 cm
690 in-house made column packed with Acclaim PepMap RPLC C18 (1.9 µm, 100 Å, Dr.
691 Maisch GmbH, Germany) working at a flow rate of 600 nl/min, using a linear gradient of
692 eluent B (20% 0.1% formic acid in water + 80% acetonitrile) in A (0.1% formic acid in
693 MilliQ water) from 4% to 10% for 5 min, 10% to 22% for 80 min, 22% to 40% for 25 min,
694 40% to 95% for 5 min, and 95% to 95% for 5 min. MS/MS analyses were performed using
695 Data-Dependent Acquisition (DDA) mode: one MS scan (mass range from 350 to 1500

696 m/z) was followed by MS/MS scans up to the top 20 most intense peptide ions from the
697 preview scan in the Orbitrap, applying a dynamic exclusion window of 120 seconds.
698
699 The raw MS files were analyzed and searched against the Mus_musculus_reviewed
700 protein database using MaxQuant (1.6.2.10). The parameters were set as follows: the
701 protein modifications were carbamidomethylation (C) (fixed), oxidation (M) (variable),
702 acetyl (Protein N-term) (variable); the enzyme specificity was set to trypsin; the maximum
703 missed cleavages were set at 2; the precursor ion mass tolerance was set at 20 ppm;
704 and the MS/MS tolerance was 20 ppm. Only highly confident identified peptides were
705 chosen for downstream protein identification analysis.
706
707 **Western blotting**
708 Western blot was performed using 4–20% Mini-PROTEAN® TGX™ precast protein
709 gels (Bio-Rad). The following antibodies: anti-CHMP5 polyclonal antibody [6], anti-
710 COL1A1 monoclonal antibody (clone E8F4L, Cell Signaling Technology, CST), anti-
711 TAGLN polyclonal antibody (cat#: AB14106, Abcam), anti-p16 INK4A monoclonal
712 antibody (clone E5F3Y, CST), anti-p21 Waf1/Cip1 monoclonal antibody (clone E2R7A,
713 CST), anti-VPS4A monoclonal antibody (clone A-11, Santa Cruz Technology), total
714 OXPHOS antibody cocktail (Abcam), anti-GAPDH monoclonal antibody (clone 14C10,
715 CST), and anti-β-Actin monoclonal antibody (clone D6A8, CST), were used.
716
717 **Quantitative PCR**

718 Total RNA was isolated from cells using Trizol reagent (Qiagen). RNA samples were
719 treated with the TURBO DNA-free™ Kit (Thermo Fisher) and equal amounts (1–2 μg)
720 were used for reverse transcriptase reaction using an iScript™ Reverse Transcription
721 Supermix (Bio-Rad). Quantitative PCR was run using the SYBR® Green Master Mix
722 on a CFX Connect™ Real-Time PCR Detection System (Bio-Rad). Gene expression
723 levels were analyzed relative to the housekeeping gene *Gapdh* and presented by $2^{-\triangle Ct}$
724 [54]. The primer sequences were used for qPCR are as following: *Chmp5,* forward, 5'-
725 ATGAGAGAGGGTCCTGCTAAG-3', reverse, 5'-CCGTGGTCTTGGTGTCCTTTA-3';
726 *H2afx*, forward, 5'-GTGGTCTCTCAGCGTTGTTC-3', reverse, 5'-CGGCC
727 TACAGGGAACTGAA-3'; *Tp53* , forward, 5'-GTCACAGCACATGACGGAGG-3', reverse,
728 5'-TCTTCCAGATGCTCGGGATAC-3'; *Gapdh*, forward 5′-TGCCAGCCTCGTCCCG
729 TAGAC-3′, reverse 5′-CCTCACCCCATTTGATGTTAG-3′; *VPS4A*, forward 5′-
730 AGAACCAGAGTGAGGGCAAGGG-3′, reverse 5′- GCACCCATCAGCTGTTCTTGCA-3′;
731 *CHMP5*, forward 5′-CCAGCCTGACTGACTGCATTGG-3′, reverse 5′-
732 TCGCAAGGCTTTCTGCTTGACC-3′; *GAPDH*, forward 5′-
733 GGAGTCCACTGGCGTCTTCAC-3′, reverse 5′-GAGGCATTGCTGATGATCTTGAGG-3′.
734

735 **Extracellular vesicle tracking**

736 The concentration and size distribution of extracellular vesicles were analyzed using
737 the NanoSight NS300 following the manufacturer's protocol (Malvern
738 Instruments). Briefly, cells were seeded in 24-well plates at the density of 1 x 10^5 cells
739 per well and cultured overnight. The next morning, cells were changed to serum-free
740 medium and incubated for 9 hrs. The medium was collected and subjected to

741 sequential centrifugation at 300 g for 10 min, 2000 g for 20 min, and 10000 g for 30
742 min. The resulting supernatant was manually injected into the instrument and run in the
743 "standard measurement" module with five captures per sample and the data were
744 processed with a detection threshold of 2.
745
746 **Live-cell imaging for cell endocytosis**
747 The *wild-type* and *Chmp5*^{Ctsk} periskeletal progenitors were incubated on ice for 10 min
748 before adding fresh medium with 2 ug/ml pHrodo™ red EGF conjugate (ThermoFisher).
749 Cells were incubated at 37 °C for 30 min and subsequently washed and changed to
750 fresh medium. Live-cell images were obtained at 1, 12, and 24 hrs using the Leica TCS
751 SP5 II laser scanning confocal microscope.
752
753 **Transmission electron microscopy**
754 *Wild-type* and *Chmp5*^{Ctsk} periskeletal progenitors were fixed in culture plates overnight
755 at 4 °C using 2.5% glutaraldehyde in 0.1 M Na cacodylate-HCl buffer (pH 7.2). After
756 washing in 0.5 M Na cacodylate-HCl buffer (pH 7.0), the cells were post-fixed for 1 hr in
757 1% osmium tetroxide (w/v) at room temperature. After post-fixation, the culture plate with
758 adherent cells were enblock stained (20 min) with 1% aqueous uranyl-acetate (w/v).
759 Culture plates were washed again in the same buffer and dehydrated through a series of
760 graded ethanol to 100% and transferred through two changes of 50/50 (v/v) SPIpon resin
761 (Structure Probe, Inc.)/100% ethanol and left overnight to infiltrate. The following morning,
762 the cell culture plates were transferred through three changes of fresh SPIpon resin to

763 finish the infiltration and embedding and finally, the plates were filled with freshly prepared
764 SPIpon resin and polymerized for 48 hrs at 70 °C.
765
766 Once fully polymerized, the plate was cut apart, and each well was plunged into liquid
767 nitrogen to separate the SPIpon epoxy block with the embedded cells from the culture
768 dish. The round epoxy disks with the embedded cells were then examined under an
769 upright light microscope, and areas of cells were cut from the disks and glued onto blank
770 microtome studs and trimmed for ultramicrotomy. Ultrathin sections (70 nm) were cut on
771 a Reichart-Jung ultramicrotome using a diamond knife. The sections were collected and
772 mounted on copper support grids and contrasted with lead citrate and uranyl acetate and
773 examined on a FEI Tecnai G2 Spirit transmission electron microscope at 100 Kv
774 accelerating voltage and images were recorded at various magnifications using a Gatan
775 2K digital camera system.
776
777 **Mitochondrial respiration**
778 Mitochondrial respiration was examined in *Chmp5*^{Ctsk} and *wild-type* periskeletal
779 progenitors using a Seahorse XF^{e}96 Extracellular Flux Analyzer (Agilent) as previously
780 described [55]. Briefly, 10000 cells per well were seeded in XF 96-well culture plates and
781 cultured overnight. The next day, cells were changed to assay medium and incubated at
782 37 °C w/o CO2 for 1 hr. The assay was carried out using the Seahorse XF Cell Mito
783 Stress Test kit with sequential injections of Oligomycin (1 μM), FCCP (1 μM), and
784 Rotenone plus Antimycin A (0.5 μM) following the manufacturer's protocol.
785

786 **Senolytic treatments**

787 For in vitro cell treatment, *Chmp5*^{Ctsk} and control cells were seeded in 96-well plates at a
788 density of 6000 cells/ well and cultured overnight. Quercetin and dasatinib were added to
789 the culture medium at a final concentration of 50 μM and 500 nM, respectively. Apoptotic
790 cells are labeled using Incucyte Annexin V Red Dye and are quantified in real time using
791 the Incucyte Live-Cell Analysis System. Six replicates were used for each group and the
792 experiment was repeated twice using cells from two different animals per group.

793

794 For in vivo treatment, the senolytic drugs quercetin and dasatinib were administered
795 intraperitoneally weekly at 50 μg/g and 5 μg/g body weight, respectively. Senolytic
796 treatment in *Chmp5*^{Ctsk} and littermate control mice started from the first week after birth
797 and mice were collected at 7-8 weeks of age for skeletal analyses. For the *Chmp5*^{Dmp1}
798 strain, treatment began the second week after birth and the animals were monitored for
799 16 weeks. ABT-263 was administered intraperitoneally to *Chmp5*^{Ctsk} and littermate control
800 mice weekly at 10 ug/g body weight, starting from the first week after birth and mice were
801 collected at 8 weeks of age for micro-CT analyses.

802

803 **Statistics**

804 All data are represented as mean ± s.d.. Normality and equal variance of the data sets
805 were tested using the Shapiro-Wilk test and the F test, respectively. The data were
806 determined to be normally distributed and have equal variance unless otherwise specified.
807 For experiments with three or more groups, statistical analysis was performed using one-
808 way or two-way ANOVA followed by multiple comparisons. For comparisons between two

809 groups, the two-tailed unpaired Student's *t*-test was applied. All analyses were performed

810 with Prism 10.1.1 (GraphPad).

811 ## References

812 1. Kaksonen M, Roux A. Mechanisms of clathrin-mediated endocytosis. Nat Rev Mol
813 Cell Biol. 2018;19(5):313-26.
814 2. Christ L, Raiborg C, Wenzel EM, Campsteijn C, Stenmark H. Cellular Functions and
815 Molecular Mechanisms of the ESCRT Membrane-Scission Machinery. Trends
816 Biochem Sci. 2017;42(1):42-56.
817 3. Luzio JP, Pryor PR, Bright NA. Lysosomes: fusion and function. Nat Rev Mol Cell Biol.
818 2007;8(8):622-32.
819 4. Hurley JH. ESCRTs are everywhere. EMBO J. 2015;34(19):2398-407.
820 5. Schmidt O, Teis D. The ESCRT machinery. Curr Biol. 2012;22(4):R116-20.
821 6. Shim JH, Xiao C, Hayden MS, Lee KY, Trombetta ES, Pypaert M, et al. CHMP5 is
822 essential for late endosome function and down-regulation of receptor signaling during
823 mouse embryogenesis. J Cell Biol. 2006;172(7):1045-56.
824 7. Kranz A, Kinner A, Kolling R. A family of small coiled-coil-forming proteins functioning
825 at the late endosome in yeast. Mol Biol Cell. 2001;12(3):711-23.
826 8. Greenblatt MB, Park KH, Oh H, Kim JM, Shin DY, Lee JM, et al. CHMP5 controls
827 bone turnover rates by dampening NF-kappaB activity in osteoclasts. J Exp Med.
828 2015;212(8):1283-301.
829 9. Adoro S, Park KH, Bettigole SE, Lis R, Shin HR, Seo H, et al. Post-translational
830 control of T cell development by the ESCRT protein CHMP5. Nat Immunol.
831 2017;18(7):780-90.
832 10. Parenti G, Medina DL, Ballabio A. The rapidly evolving view of lysosomal storage
833 diseases. EMBO Mol Med. 2021;13(2):e12836.

834 11. Morishita K, Petty RE. Musculoskeletal manifestations of mucopolysaccharidoses.
835 Rheumatology (Oxford). 2011;50 Suppl 5:v19-25.
836 12. Clarke LA, Hollak CE. The clinical spectrum and pathophysiology of skeletal
837 complications in lysosomal storage disorders. Best Pract Res Clin Endocrinol Metab.
838 2015;29(2):219-35.
839 13. Miller BS, Fung EB, White KK, Lund TC, Harmatz P, Orchard PJ, et al. Persistent
840 bone and joint disease despite current treatments for mucopolysaccharidosis types I,
841 II, and VI: Data from a 10-year prospective study. J Inherit Metab Dis. 2023;46(4):695-
842 704.
843 14. Yang W, Wang J, Moore DC, Liang H, Dooner M, Wu Q, et al. Ptpn11 deletion in a
844 novel progenitor causes metachondromatosis by inducing hedgehog signalling.
845 Nature. 2013;499(7459):491-5.
846 15. Debnath S, Yallowitz AR, McCormick J, Lalani S, Zhang T, Xu R, et al. Discovery of
847 a periosteal stem cell mediating intramembranous bone formation. Nature.
848 2018;562(7725):133-9.
849 16. Shi R, He L, Ren J, Zhou B, Hou G, Zhou B, et al. A migratory stem cell population
850 for musculoskeletal enveloping tissues and the bone. SSRN 3281656, 2018.
851 (http://dx.doi.org/10.2139/ssrn.3281656).
852 17. Logan M, Martin JF, Nagy A, Lobe C, Olson EN, Tabin CJ. Expression of Cre
853 Recombinase in the developing mouse limb bud driven by a Prxl enhancer. Genesis.
854 2002;33(2):77-80.

855 18. Ono N, Ono W, Mizoguchi T, Nagasawa T, Frenette PS, Kronenberg HM.
856 Vasculature-associated cells expressing nestin in developing bones encompass early
857 cells in the osteoblast and endothelial lineage. Dev Cell. 2014;29(3):330-9.
858 19. Maes C, Kobayashi T, Selig MK, Torrekens S, Roth SI, Mackem S, et al. Osteoblast
859 precursors, but not mature osteoblasts, move into developing and fractured bones
860 along with invading blood vessels. Dev Cell. 2010;19(2):329-44.
861 20. Lim J, Shi Y, Karner CM, Lee SY, Lee WC, He G, et al. Dual function of Bmpr1a
862 signaling in restricting preosteoblast proliferation and stimulating osteoblast activity
863 in mouse. Development. 2016;143(2):339-47.
864 21. Lim J, Burclaff J, He G, Mills JC, Long F. Unintended targeting of Dmp1-Cre reveals
865 a critical role for Bmpr1a signaling in the gastrointestinal mesenchyme of adult mice.
866 Bone Res. 2017;5:16049.
867 22. Matic I, Matthews BG, Wang X, Dyment NA, Worthley DL, Rowe DW, et al. Quiescent
868 Bone Lining Cells Are a Major Source of Osteoblasts During Adulthood. Stem Cells.
869 2016;34(12):2930-42.
870 23. Ge X, Tsang K, He L, Garcia RA, Ermann J, Mizoguchi F, et al. NFAT restricts
871 osteochondroma formation from entheseal progenitors. JCI Insight.
872 2016;1(4):e86254.
873 24. Birch J, Gil J. Senescence and the SASP: many therapeutic avenues. Genes Dev.
874 2020;34(23-24):1565-76.
875 25. Romanello M, Piatkowska E, Antoniali G, Cesaratto L, Vascotto C, Iozzo RV, et al.
876 Osteoblastic cell secretome: a novel role for progranulin during risedronate treatment.
877 Bone. 2014;58:81-91.

878 26. Davies OG, Cox SC, Azoidis I, McGuinness AJA, Cooke M, Heaney LM, et al.
879 Osteoblast-Derived Vesicle Protein Content Is Temporally Regulated During
880 Osteogenesis: Implications for Regenerative Therapies. Front Bioeng Biotechnol.
881 2019;7:92.
882 27. Zhu Y, Tchkonia T, Pirtskhalava T, Gower AC, Ding H, Giorgadze N, et al. The
883 Achilles' heel of senescent cells: from transcriptome to senolytic drugs. Aging Cell.
884 2015;14(4):644-58.
885 28. Hickson LJ, Langhi Prata LGP, Bobart SA, Evans TK, Giorgadze N, Hashmi SK, et
886 al. Senolytics decrease senescent cells in humans: Preliminary report from a clinical
887 trial of Dasatinib plus Quercetin in individuals with diabetic kidney disease.
888 EBioMedicine. 2019;47:446-56.
889 29. Tse C, Shoemaker AR, Adickes J, Anderson MG, Chen J, Jin S, et al. ABT-263: a
890 potent and orally bioavailable Bcl-2 family inhibitor. Cancer Res. 2008;68(9):3421-8.
891 30. Chang J, Wang Y, Shao L, Laberge RM, Demaria M, Campisi J, et al. Clearance of
892 senescent cells by ABT263 rejuvenates aged hematopoietic stem cells in mice. Nat
893 Med. 2016;22(1):78-83.
894 31. Martini H, Passos JF. Cellular senescence: all roads lead to mitochondria. FEBS J.
895 2023;290(5):1186-202.
896 32. Park JT, Lee YS, Cho KA, Park SC. Adjustment of the lysosomal-mitochondrial axis
897 for control of cellular senescence. Ageing Res Rev. 2018;47:176-82.
898 33. Gorgoulis V, Adams PD, Alimonti A, Bennett DC, Bischof O, Bishop C, et al. Cellular
899 Senescence: Defining a Path Forward. Cell. 2019;179(4):813-27.

900 34. Korolchuk VI, Miwa S, Carroll B, von Zglinicki T. Mitochondria in Cell Senescence: Is
901 Mitophagy the Weakest Link? EBioMedicine. 2017;21:7-13.
902 35. Birch J, Passos JF. Targeting the SASP to combat ageing: Mitochondria as possible
903 intracellular allies? Bioessays. 2017;39(5).
904 36. Paramos-de-Carvalho D, Jacinto A, Saude L. The right time for senescence. Elife.
905 2021;10.
906 37. Wiley CD, Campisi J. The metabolic roots of senescence: mechanisms and
907 opportunities for intervention. Nat Metab. 2021;3(10):1290-301.
908 38. Martini H, Passos JF. Cellular senescence: all roads lead to mitochondria. FEBS J.
909 2022.
910 39. Vild CJ, Li Y, Guo EZ, Liu Y, Xu Z. A novel mechanism of regulating the ATPase
911 VPS4 by its cofactor LIP5 and the endosomal sorting complex required for transport
912 (ESCRT)-III protein CHMP5. J Biol Chem. 2015;290(11):7291-303.
913 40. Yang Z, Vild C, Ju J, Zhang X, Liu J, Shen J, et al. Structural basis of molecular
914 recognition between ESCRT-III-like protein Vps60 and AAA-ATPase regulator Vta1
915 in the multivesicular body pathway. J Biol Chem. 2012;287(52):43899-908.
916 41. Rodger C, Flex E, Allison RJ, Sanchis-Juan A, Hasenahuer MA, Cecchetti S, et al.
917 De Novo VPS4A Mutations Cause Multisystem Disease with Abnormal
918 Neurodevelopment. Am J Hum Genet. 2020;107(6):1129-48.
919 42. Salazar JC, Duhnam-Ems S, La Vake C, Cruz AR, Moore MW, Caimano MJ, et al.
920 Activation of human monocytes by live Borrelia burgdorferi generates TLR2-
921 dependent and -independent responses which include induction of IFN-beta. PLoS
922 Pathog. 2009;5(5):e1000444.

923 43. Thiebaut R, Esmiol S, Lecine P, Mahfouz B, Hermant A, Nicoletti C, et al.
924 Characterization and Genetic Analyses of New Genes Coding for NOD2 Interacting
925 Proteins. PLoS One. 2016;11(11):e0165420.
926 44. Dai GC, Wang H, Ming Z, Lu PP, Li YJ, Gao YC, et al. Heterotopic mineralization
927 (ossification or calcification) in aged musculoskeletal soft tissues: A new candidate
928 marker for aging. Ageing Res Rev. 2024;95:102215.
929 45. Lu Y, Xie Y, Zhang S, Dusevich V, Bonewald LF, Feng JQ. DMP1-targeted Cre
930 expression in odontoblasts and osteocytes. J Dent Res. 2007;86(4):320-5.
931 46. Rodda SJ, McMahon AP. Distinct roles for Hedgehog and canonical Wnt signaling in
932 specification, differentiation and maintenance of osteoblast progenitors. Development.
933 2006;133(16):3231-44.
934 47. Nakamura T, Imai Y, Matsumoto T, Sato S, Takeuchi K, Igarashi K, et al. Estrogen
935 prevents bone loss via estrogen receptor alpha and induction of Fas ligand in
936 osteoclasts. Cell. 2007;130(5):811-23.
937 48. Bonetto A, Andersson DC, Waning DL. Assessment of muscle mass and strength in
938 mice. Bonekey Rep. 2015;4:732.
939 49. Takeshita H, Yamamoto K, Nozato S, Inagaki T, Tsuchimochi H, Shirai M, et al.
940 Modified forelimb grip strength test detects aging-associated physiological decline in
941 skeletal muscle function in male mice. Sci Rep. 2017;7:42323.
942 50. Langmead B, Salzberg SL. Fast gapped-read alignment with Bowtie 2. Nat Methods.
943 2012;9(4):357-9.
944 51. Dobin A, Davis CA, Schlesinger F, Drenkow J, Zaleski C, Jha S, et al. STAR: ultrafast
945 universal RNA-seq aligner. Bioinformatics. 2013;29(1):15-21.

946 52. Trapnell C, Hendrickson DG, Sauvageau M, Goff L, Rinn JL, Pachter L. Differential
947 analysis of gene regulation at transcript resolution with RNA-seq. Nat Biotechnol.
948 2013;31(1):46-53.
949 53. Fabregat A, Sidiropoulos K, Viteri G, Forner O, Marin-Garcia P, Arnau V, et al.
950 Reactome pathway analysis: a high-performance in-memory approach. BMC
951 Bioinformatics. 2017;18(1):142.
952 54. Schmittgen TD, Livak KJ. Analyzing real-time PCR data by the comparative C(T)
953 method. Nat Protoc. 2008;3(6):1101-8.
954 55. Fiorese CJ, Schulz AM, Lin YF, Rosin N, Pellegrino MW, Haynes CM. The
955 Transcription Factor ATF5 Mediates a Mammalian Mitochondrial UPR. Curr Biol.
956 2016;26(15):2037-43.
957

958 ## Figure Legends

959 **Fig. 1. Ablation of *Chmp5* in mouse osteogenic lineage cells causes aberrant bone**
960 **formation.**

961 (**A**) Micro-CT and H&E staining showing periskeletal overgrowth in *Chmp5*^{Ctsk} mice in
962 comparison with *Chmp5*$^{fl/fl}$ mice at 7 weeks of age. Dot line representing the approximate
963 bone border. *n* = 10 animals per group. (**B**) Micro-CT images displaying periskeletal
964 overgrowth in the ankle and foot in *Chmp5*^{Ctsk} versus *Chmp5*$^{fl/fl}$ mice at one year of age.
965 *n* = 4 animals per group. (**C**) Alizarin red staining of skeletal preparations on postnatal
966 day 10. *n* = 4 mice per group, arrows indicating periskeletal bone overgrowth. (**D**) Three-
967 point test showing femur bone stiffness and ultimate stress (fracture stress) in *Chmp5*^{Ctsk}
968 and *Chmp5*$^{fl/fl}$ mice. *n* = 5 male animals per group. Similar changes observed in both
969 sexes. (**E**) Confocal images mapping *Ctsk*$^{+}$ (GFP^{+}) progenitors in periskeletal tissues in
970 *Chmp5*$^{Ctsk/+}$;*Rosa26*$^{mTmG/+}$ and *Chmp5*^{Ctsk};*Rosa26*$^{mTmG/+}$ mice at 2 weeks of age.
971 Asterisks indicating periskeletal overgrowths; dot-line representing the approximate bone
972 border. *n* = 4 animals each group. (**F**) X-ray images demonstrating progressive cortical
973 bone expansion (arrows) and decreased skeletal muscle mass (asterisks) in *Chmp5*^{Dmp1}
974 in comparison with *Chmp5*$^{fl/fl}$ mice. *n* = 3, 3, 10, 8 animals per group for 3 weeks, 5 weeks,
975 10 weeks, and 1 year of age, respectively. (**G**) Micro-CT analyses displaying cortical bone
976 expansion in *Chmp5*^{Dmp1} relative to *Chmp5*$^{fl/fl}$ mice at 10 weeks of age. *n* = 6 *Chmp5*$^{fl/fl}$
977 and 5 *Chmp5*^{Dmp1} male mice, similar changes found in both genders. (**H**) Skeletal muscle
978 mass in *Chmp5*^{Dmp1} compared to *Chmp5*$^{fl/fl}$ mice at 10-12 weeks of age. *n* = 4 animals
979 (male) per group, similar changes found in both genders. (**I**) Hindlimb abduction of
980 *Chmp5*^{Dmp1} mice in comparison with *Chmp5*$^{fl/fl}$ littermate controls at 10 weeks of age.

981 More than 20 animals per group observed. (**J**) Four-limb handing time (*n* = 10 per group,
982 pooled data from both sexes), and forelimb pull strength (*n* = 6 per group, male mice) in
983 *Chmp5*^{Dmp1} compared to *Chmp5*$^{fl/fl}$ mice at 10-12 weeks of age. Similar changes found
984 in both genders. All data are mean ± s.d.; two-tailed unpaired Student's *t*-test. Scale bars,
985 1 mm for micro-CT and skeletal preparation images, 200 μm for histological images, and
986 10 mm in panel (**F**).
987
988 **Fig. 2. CHMP5 restricts osteogenesis in skeletal progenitor cells.**
989 (**A**) Flow cytometry showing the strategy for sorting CD45$^-$;CD31$^-$;GFP$^+$ and
990 CD45$^-$;CD31$^-$;GFP$^-$ periskeletal progenitors from periskeletal tissues of
991 *Chmp5*$^{Ctsk/+}$*;Rosa26*$^{mTmG/+}$ and *Chmp5*^{Ctsk}*;Rosa26*$^{mTmG/+}$ mice at 2 weeks of age. *n* = 10
992 mice per group. (**B**) Quantitative PCR determining the expression of *Chmp5* in *Chmp5*^{Ctsk}
993 relative to *Chmp5*$^{Ctsk/+}$ periskeletal progenitors. *n* = 6 mice per group. (**C**) Alizarin red
994 staining, von Kossa staining and alkaline phosphatase activity assay determining
995 osteogenesis in *Chmp5*^{Ctsk} compared to *Chmp5*$^{Ctsk/+}$ periskeletal progenitors. *n* = 3
996 replicates each group, representative results of cells from 3 different mice per group. (**D**)
997 Western blot confirming *Chmp5* deletion in mouse MC3T3-E1 cells by lentiviral
998 CRISPR/CAS9. (**E**) Alizarin red staining demonstrating osteogenesis in MC3T3-E1 cells
999 with or without *Chmp5* deletion by lentiviral CRISPR/CAS9. *n* = 4 replicates per group,
1000 experiments repeated twice for each time point. **(F)** Ingenuity pathway analysis of RNA-
1001 seq data showing increased activity of osteoblast differentiation in *Chmp5*^{Ctsk} vs.
1002 *Chmp5*$^{Ctsk/+}$ periskeletal progenitors. All data are mean ± s.d.; two-tailed unpaired
1003 Student's *t*-test.

1004

1005 **Fig. 3. CHMP5 controls skeletal progenitor cell senescence.**

1006 (**A**) Cell number counting and AlamarBlue assay determining cell proliferation in
1007 *Chmp5*^{Ctsk} and *Chmp5*$^{Ctsk/+}$ periskeletal progenitors from 2-week-old animals. *n* = 3
1008 replicates per group per time point; experiments repeated 3 times using cells from 3
1009 different mice. (**B**) Volcano plot of RNA-seq data showing differentially expressed genes
1010 in *Chmp5*^{Ctsk} vs. *Chmp5*$^{Ctsk/+}$ periskeletal progenitors. *n* = 3 per group with cells from 3
1011 different animals. (**C**) ConsensusPathDB gene set enrichment analysis of RNA-seq data
1012 showing positive enrichment of genes in multiple molecular pathways related to cell
1013 senescence (Reactome) in *Chmp5*^{Ctsk} relative to *Chmp5*$^{Ctsk/+}$ periskeletal progenitors. (**D**)
1014 Western blot determining the expression of p16 and p21 proteins in *Chmp5*^{Ctsk} compared
1015 to *wild-type* (control) periskeletal progenitors. The numbers above lanes indicating the
1016 intensity of the p16 or p21 band relative to that of *Control* cells after normalization by β-
1017 Actin. Results repeated 3 times with cells from 3 different animals. (**E**) Immunostaining of
1018 γH2AX and quantification of γH2AX^{+};GFP^{+} cells in the periosteum and periskeletal
1019 overgrowth in *Chmp5*$^{Ctsk/+}$*;Rosa26*$^{mTmG/+}$ and *Chmp5*^{Ctsk}*;Rosa26*$^{mTmG/+}$ mice, respectively.
1020 *n* = 3 with tissues from 3 different animals per group. (**F**) Gross image demonstrating
1021 aging-related phenotypes in *Chmp5*^{Ctsk} compared to *Chmp5*$^{Ctsk/+}$ mice at 1 year of age.
1022 Images are representative of 5 animals per group. (**G**) Cell cycle analysis in ATDC5 cells
1023 with or without *Chmp5* deletion. *n* = 3 replicates per group, results repeated twice. All data
1024 are mean ± s.d.; 2-way ANOVA followed by multiple comparisons or two-tailed unpaired
1025 Student's *t*-test (E).

1026

1027 **Fig. 4. Secretory phenotype of *Chmp5*-deficient skeletal progenitors.**

1028 (**A**) GSEA of RNA-seq data showing positive enrichment of genes associated with the
1029 molecular pathway of senescence-associated secretory phenotype (Reactome database)
1030 in *Chmp5*^{Ctsk} relative to *Chmp5*$^{Ctsk/+}$ periskeletal progenitors. (**B**) Confocal images
1031 showing and quantifying extracellular vesicles (arrowheads) around *Chmp5*^{Ctsk}
1032 periskeletal progenitors. Images are representative of 30 cells from 3 animals per group.
1033 Scale bars, 10 μm. (**C** and **D**) Nanoparticle tracking analysis of extracellular vesicles in
1034 culture medium of *Chmp5*^{Ctsk} and *wild-type* periskeletal progenitors. Data pooled from 3
1035 replicates per group, 5 reads for each; repeated twice using cells from 2 mice per group.
1036 (**E**) Cell number counting determining cell proliferation in ATDC5 cells treated with culture
1037 supernatant from *Chmp5*-deficient or *Chmp5*-sufficient cells. *n* = 3 per group per time
1038 point, repeated twice. (**F** and **G**) Cell number counting and alizarin red staining examining
1039 cell proliferation (**F**) and osteogenesis (**G**) in neighboring CD45^{-};CD31^{-};GFP^{-} progenitors
1040 sorted from periskeletal tissues of *Chmp5*^{Ctsk}*;Rosa26*$^{mTmG/+}$ or *Ctsk-Cre;Rosa26*$^{mTmG/+}$
1041 mice. *n* = 3 replicates per group per time point, repeated 3 times using cells from 3
1042 different animals. (**H**) Volcano plot showing differentially secreted protein in supernatants
1043 of *Chmp5*^{Ctsk} vs. *wild-type* periskeletal progenitors analyzed by Nano LC-MS/MS. *n* = 3
1044 with cells from 3 different animals per group. (**I**) Western blot verifying the increase in
1045 COL1A1 and TAGLN proteins in supernatants of *Chmp5*^{Ctsk} relative to *wild-type*
1046 periskeletal progenitors. Commas blue stain as the loading control. Results repeated 3
1047 times using cells from 3 different mice each group. All data are mean ± s.d.; two-tailed
1048 unpaired Student's *t*-test for comparison of two groups or 2-way ANOVA followed by
1049 multiple comparisons.

1050

1051 **Fig. 5. Senolytic treatment mitigates musculoskeletal pathologies in *Chmp5* 1052 conditional knockout mice.**

1053 (**A**) Incucyte live-cell apoptosis analysis of *Chmp5*^{Ctsk} and *wild-type* periskeletal 1054 progenitors treated with 50 μM Quercetin and 500 nM dasatinib (Q + D) and labeled by 1055 Annexin V. *n* = 6 for each group, experiment repeated twice using cells from different 1056 animals. (**B**) Gross images, radiography, and histology (H&E) respectively demonstrating 1057 hindlimb abduction and periskeletal bone overgrowth (arrows or dot-line) in *Chmp5*^{Ctsk} in 1058 comparison with *Chmp5*$^{fl/fl}$ mice after treatment with Q + D or vehicle PEG400 weekly for 1059 7 weeks. *n* = 8-10 mice per group. Continuous lines in H&E images indicating an 1060 approximate edge of the cortical bone and dot lines indicating the edge of periskeletal 1061 overgrowing bones. Scale bars, 100 μm. (**C**) Four-limb hanging time and forelimb pull 1062 strength in *Chmp5*^{Dmp1} and *Chmp5*$^{fl/fl}$ mice after treatment with Q + D or the vehicle 1063 PEG400 weekly for 16 weeks. *n* = 12 animals per group for hanging time test pooled from 1064 both genders; *n* = 7 male mice per group for the forelimb pull strength test, similar changes 1065 found in both genders. (**D**) Gross images showing hindlimb abduction in *Chmp5*^{Dmp1} 1066 compared to *Chmp5*$^{fl/fl}$ mice after treatment with Q + D or the vehicle PEG400. *n* = 12 1067 animals per group. (**E**) Gross image and Micro-CT analysis demonstrating femur and 1068 cortical bone thickness in *Chmp5*^{Dmp1} mice after treatment with Q + D or the vehicle 1069 PEG400. *n* = 5 male mice per group, similar changes found in both genders. Scale bar, 1070 1 mm. (**F**) Micro-CT images showing periskeletal bone overgrowth in *Chmp5*^{Ctsk} in 1071 comparison with *Chmp5*$^{fl/fl}$ mice after treatment with ABT-263 or vehicle weekly for 8 1072 weeks. *n* = 4 mice per group, Scale bars, 2 mm. All data are mean ± s.d.; 2-way ANOVA

1073 followed by multiple comparisons or two-tailed unpaired Student's *t*-test for comparison
1074 of two groups.
1075
1076 **Fig. 6. CHMP5 is essential for endolysosomal functions and maintaining VPS4A**
1077 **protein in skeletal progenitors.**
1078 (**A**) Representative confocal images demonstrating abnormally enlarged vesicles in
1079 cultured *Chmp5*^{Ctsk} relative to *wild-type* periskeletal progenitors. Abnormal cells identified
1080 by containing enlarged GFP^{+} vesicles. *n* = 200 cells from 3 mice per group. (**B**) Schematic
1081 showing molecular markers utilized to analyze the endocytic pathway. (**C**) Representative
1082 confocal images showing LAMP1 immunostaining in *Chmp5*^{Ctsk} and *wild-type* periskeletal
1083 progenitors. *n* = 20 cells per group. (**D**) Quantification of LAMP1^{+} vesicles in ATDC5 cells
1084 with or without *Chmp5* depletion. *n* = 93, 66 cells, respectively. (**E**) Representative
1085 confocal images showing RAB7 immunostaining in *Chmp5*^{Ctsk} and *wild-type* periskeletal
1086 progenitors. *n* = 15 cells per genotype. (**F**) Quantification of RAB7^{+} vesicles in ATDC5
1087 cells with or without *Chmp5* depletion. *n* = 94, 92 cells, respectively. (**G)** Transmission
1088 electron microscopy showing the accumulation of multivesicular body-like structures
1089 (arrows) and lysosome-like structures (arrowheads) in *Chmp5*^{Ctsk} relative to *wild-type*
1090 periskeletal progenitors. *n* = 30 cells per group. (**H**) Confocal live cell images
1091 demonstrating delayed degradation of the EGF conjugate in *Chmp5*^{Ctsk} vs. *wild-type*
1092 periskeletal progenitors. *n* = 10 cells each group per time point. (**I**) Volcano plot of
1093 proteomic analysis showing differentially expressed proteins in *Chmp5*^{Ctsk} vs. *wild-type*
1094 periskeletal progenitors. *n* = 3 with cells from 3 different animals. (**J**) Western blot verifying
1095 the decrease in VPS4A protein in *Chmp5*^{Ctsk} vs. *wild-type* periskeletal progenitors. The

1096 numbers above lanes indicating the intensity of the VPS4A band relative to that of *wild-*
1097 *type* cells after normalization by β-Actin. Results repeated 3 times with cells from 3
1098 different mice each group. All data are mean ± s.d.; Mann-Whitney test for the comparison
1099 of the vesicle number and two-tailed unpaired Student's *t*-test for the comparison of the
1100 vesicle size in (**D**) and (**F**). Scale bars, 10 μm except (**G**) as indicated.
1101
1102 **Fig. 7. Mitochondrial dysfunction is responsible for cell senescence in *Chmp5*-**
1103 **deleted skeletal progenitors.**
1104 (**A**) GSEA of RNA--seq data reporting positive enrichment of genes associated with the
1105 molecular pathway of oxidative stress-induced senescence in *Chmp5*^{Ctsk} relative to
1106 *Chmp5*$^{Ctsk/+}$ periskeletal progenitors. (**B**) Confocal fluorescence images showing
1107 intracellular ROS (CellROX Deep Red) and mitochondria (TMRE) in *Chmp5*^{Ctsk} vs. *wild-*
1108 *type* periskeletal progenitors. Images are representative of 30 cells per group. Scale bars,
1109 15 μm. The graph on the right shows the quantification of the fluorescence intensity of
1110 CellROX Deep Red. *n* = 10 each group, results repeated twice. (**C**) Quantification of
1111 TMRE fluorescence intensity in *Chmp5*-sufficient and *Chmp5*-deficient ATDC5 cells. *n* =
1112 12 for each group, repeated 3 times. (**D**) Western blotting determining the expression of
1113 mitochondrial OXPHOS proteins NDUF88, SDHB, MT-CO1, UQCRC2, and ATF5A in
1114 *Chmp5*-deficient compared to *Chmp5*-sufficient ATDC5 cells. Experiment repeated twice.
1115 (**E**) Cell number counting to determine cell proliferation in galactose medium. *n* = 6
1116 replicates per group, repeated three times. (**F**) Seahorse mitochondrial stress test
1117 showing mitochondrial respiratory capacity and extracellular acidification rate in
1118 *Chmp5*^{Ctsk} relative to *wild-type* periskeletal progenitors. Data pooled from cells of 3 mice,

1119 8 replicates for each sample. (**G**) Cell number counting and AlamarBlue assay
1120 determining cell proliferation in ATDC5 cells with or without *Chmp5* depletion after
1121 treatment with the antioxidant *N*-Acetyl cysteine. *n* = 3 or 12 each group for cell number
1122 counting or AlamarBlue assay, respectively; results repeated 3 times. (**H**) Schematic
1123 showing the function of CHMP5 in maintaining VPS4A protein and endolysosomal
1124 homeostasis and restricting cell senescence and osteogenesis in skeletal progenitors. All
1125 data are mean ± s.d.; two-tailed unpaired Student's *t*-test, except the Mann-Whitney test
1126 in panel (**E**).
1127

1128 ## Supplementary Figure Legends

1129 **Fig. S1. CHMP5 restricts bone formation in osteogenic lineage cells.**

1130 (**A**) Alizarin red staining of skeletal preparations on postnatal day 2. *n* = 4 mice per group.
1131 Scale bar, 1 mm. (**B**) Confocal images of *Rosa26*$^{mTmG/+}$ (Cre^{-}) control mice. Related to
1132 Fig. 1E. Scale bar, 200 μm. (**C**) Tartrate-resistant acid phosphatase (TRAP) staining
1133 demonstrating the absence of osteoclasts in peri-skeletal overgrowth (asterisk) of
1134 *Chmp5*^{Ctsk} mice at 2 weeks of age. TRAP^{+} osteoclasts in the bone marrow as positive
1135 control; dot-line representing approximate border between peri-skeletal overgrowth and
1136 the bone at femoral condyle of the knee. Images are representative of 3 animals per group.
1137 Scale bar, 200 μm. (**D**) Gross image and measurement of femur thickness showing bone
1138 expansion in *Chmp5*^{Dmp1} versus *Chmp5*$^{fl/fl}$ mice at 10 weeks of age. *n* = 13 *Chmp5*$^{fl/fl}$ and
1139 12 *Chmp5*^{Dmp1} mice. Scale bar, 1 mm. (**E**) H&E histology showing bone expansion at the
1140 endosteum (arrows) in *Chmp5*^{Dmp1} mice. The left images showing the midshaft and the
1141 right images showing the metaphysis of the femur bone. Images are representative of 3
1142 mice per group. Scale bars, 0.5 mm. Data are mean ± s.d.; two-tailed unpaired Student's
1143 *t*-test.

1144

1145 **Fig. S2. Sorting of CD45^{-};CD31^{-};CTSK^{+} periskeletal progenitors.**

1146 (**A**) Unstained cells from *Rosa26-mTmG*$^{fl/+}$ mice as a negative control for sorting
1147 CD45^{-};CD31^{-};CTSK^{+} skeletal progenitors. Related to Fig. 2A. (**B**) Quantification of
1148 CD45^{-};CD31^{-};GFP^{+} and CD45^{-};CD31^{-};GFP^{-} cell population in samples of
1149 *Chmp5*^{Ctsk}*;Rosa26*$^{mTmG/+}$ mice. *n* = 10 mice per group.

1150

1151 **Fig. S3. Cell apoptosis is not the main cause of the decreased proliferative rate in**
1152 ***Chmp5*-deficient skeletal progenitors.**
1153 (**A**) Annexin V stain examining cellular apoptosis in *Chmp5*^{Ctsk} and *Chmp5*$^{Ctsk/+}$
1154 periskeletal progenitors. *n* = 3 replicates each group; repeated twice using cells from 2
1155 mice per group. (**B**) TUNEL staining and quantification of TUNEL^{+} cells (%) in the
1156 periskeletal tissues of *Chmp5*^{Ctsk} and *Chmp5*$^{Ctsk/+}$ mice. Arrows indicating positive cells in
1157 periskeletal overgrowth in *Chmp5*^{Ctsk} mice, dot-line representing approximate border
1158 between periskeletal overgrowth and bone in the femoral condyle of the knee; *n* = 3
1159 animals per group; scale bars, 100 μm. (**C**) GSEA of RNA-seq data showing significant
1160 enrichment of SAUL_SEN_MAYO and KAMMINGA_SENESCENCE genesets in
1161 *Chmp5*^{Ctsk} relative to *Chmp5*$^{Ctsk/+}$ periskeletal progenitors. (**D**) *Cdkn1a* and *Cdkn2a* mRNA
1162 levels in *Chmp5*^{Ctsk} and *Chmp5*$^{Ctsk/+}$ periskeletal progenitors according to RNA-seq data.
1163 *n* = 3 per group with cells from 3 different animals. (**E**) Western blot confirming deletion
1164 of *Chmp5* in ATDC5 cells by lentiviral CRISPR/CAS9. (**F**) Cell number counting
1165 determining cell proliferation in ATDC5 cells after deleting *Chmp5* by lentiviral
1166 CRISPR/CAS9. *n* = 4 replicates per group per time point, experiment repeated three times.
1167 (**G**) Annexin V-PI stain analyzing cellular apoptosis in ATDC5 cells with or without *Chmp5*
1168 deletion. *n* = 3 replicates for each group, repeated 3 times. (**H**) Cell number counting
1169 determining cell proliferation in ATDC5 cells with or without *Chmp5* deletion after
1170 treatment with the pan-caspase inhibitor Q-VD-OPh. *n* = 3 replicates of each group each
1171 dose, repeated twice. All data are mean ± s.d.; two-tailed Student's *t*-test for comparison
1172 of two groups or 2-way ANOVA followed by multiple comparisons.
1173

1174 **Fig. S4. Secretory phenotype of *Chmp5*-deficient skeletal progenitors.**

1175 (**A**) Nanoparticle tracking analysis showing the size distribution of extracellular vesicles
1176 in *Chmp5*^{Ctsk} and *wild-type* skeletal progenitors. Data pooled from 3 replicates, 5 reads
1177 for each; repeated twice using cells from 2 mice; D10, D50, and D90 indicating percent
1178 undersize, for example D50 = 229 nm representing that 50% of vesicles are 229 nm or
1179 smaller. (**B**) Alizarin red staining and quantification showing osteogenesis in coculture of
1180 *Chmp5*^{Ctsk} and *wild-type* periskeletal progenitors. *n* = 3 replicates per group, repeated
1181 twice using cells from 2 different animals. (**C**) AlarmaBlue assay examining cell
1182 proliferation in neighboring CD45^{-};CD31^{-};GFP^{-} progenitors sorted from periskeletal
1183 tissues of *Chmp5*^{Ctsk}*;Rosa26*$^{mTmG/+}$ or *Ctsk-Cre;Rosa26*$^{mTmG/+}$ mice. *n* = 12 replicates per
1184 group per time-point, repeated 3 times using cells from 3 animals. (**D**) Alizarin red staining
1185 determining osteogenesis in neighboring CD45^{-};CD31^{-};GFP^{-} progenitors sorted from
1186 periskeletal tissues of *Chmp5*^{Ctsk}*;Rosa26*$^{mTmG/+}$ or *Ctsk-Cre;Rosa26*$^{mTmG/+}$ mice after
1187 induction in osteogenic medium for 3 weeks. *n* = 3 replicates per group per time point,
1188 repeated 3 times using cells from 3 animals. (**E**) Immunostaining and quantification of cell
1189 proliferation marker Ki-67 in the periskeletal tissues around the knee of *Chmp5*^{Ctsk} and
1190 *Chmp5*$^{Ctsk/+}$ mice. *n* = 3 animals per group; dot-line representing the approximate border
1191 between the periskeletal overgrowth and the bone in the femoral condyle; scale bars, 100
1192 μm. (**F**) Heatmap of LC-MS/MS results showing differentially secreted proteins in
1193 supernatants of *Chmp5*^{Ctsk} relative to *wild-type* skeletal progenitors. *n* = 3 with cells from
1194 3 different animals per group for Nano LC-MS/MS analysis. All data are mean ± s.d., 2-
1195 way ANOVA followed by multiple comparisons or two-tailed unpaired Student's *t*-test for
1196 2-group comparison.

1197

1198 **Fig. S5. Additional x-ray images of *Chmp5^{Ctsk}* mice after treatment with Q + D or the**

1199 **vehicle PEG400 for 7 weeks**. Arrows indicating periskeletal bone overgrowths.

1200

1201 **Fig. S6. CHMP5 is essential for endolysosomal functions and maintaining VPS4A**

1202 **protein in skeletal progenitors.**

1203 (**A**) Representative confocal fluorescence images and quantification of the fluorescence

1204 intensity of LysoTracker Red DND-99 in *Chmp5^{Ctsk}* compared to *wild-type* periskeletal

1205 progenitors. *n* = 11 replicates per group for quantitative analysis; repeated 3 times using

1206 cells from 3 mice. Scale bars, 50 μm. (**B**) Isotype controls for immunofluorescence

1207 staining. Scale bars, 20 μm. (**C**) Co-localization of LAMP1 and RAB7 in *Chmp5*-sufficient

1208 or *Chmp5*-deficient ATDC5 cells. Scale bars, 10 μm. (**D**) Colocalization analysis of

1209 LAMP1 and RAB7 performed by the ImageJ Coloc2 programme and Pearson's R value

1210 (above threshold) shown, *n* = 20 cells per group. (**E**) Representative confocal images of

1211 immunostaining for early endosome marker EEA1, cycling endosome marker RAB11, and

1212 trans-Golgi network marker TGN38 in *Chmp5^{Ctsk}* vs. *wild-type* periskeletal progenitors. *n*

1213 = 30 cells per group. Scale bars, 10 μm (EEA1), 20 μm (RAB11), 25 μm (TGN38). (**F**)

1214 RNA-seq data showing *Vps4a* mRNA expression in *Chmp5^{Ctsk}* vs. *Chmp5$^{Ctsk/+}$*

1215 periskeletal progenitors. *n* = 3 with cells from 3 different animals for each group. (**G**)

1216 Western blot showing that CHMP5 and VPS4A protein expression after transfection of

1217 CHMP5 or empty vector in HEK-293T cells. Experiments repeated 3 times with

1218 independent cells and transfections at different times. (**H**) Quantitative PCR showing the

1219 expression of *CHMP5* and *VPS4A* mRNA after transfecting CHMP5 or empty vector in

1220 HEK-293T cells. *n* = 3 replicates for each group, experiments repeated 3 times with
1221 independent cells and transfections at different times. All data shown as mean ± s.d.; two-
1222 tailed unpaired Student's *t*-test.
1223
1224 **Fig. S7. Mitochondrial dysfunction and activation of DNA damage-induced**
1225 **senescence in *Chmp5*-deficient skeletal progenitors.**
1226 (**A**) Representative TMRE confocal images showing accumulation of mitochondria in
1227 *Chmp5*^{Ctsk} periskeletal progenitors. *n* = 30 cells per group, scale bars, 25 μm. (**B**)
1228 Confocal fluorescence imaging mapping intracellular ROS (CellROX Deep Red) and
1229 mitochondria (MitoTracker Green) in ATDC5 cells with or without *Chmp5* depletion. *n* =
1230 20 cells for each group; scale bars, 10 μm. The right histogram showing the quantification
1231 of CellROX Deep Red in ATDC5 cells by flow cytometry. *n* = 3 per group, experiment
1232 repeated twice. (**C**) GSEA of RNA-seq data showing positive enrichment of genes
1233 associated with the molecular pathway of DNA damage-induced senescence in
1234 *Chmp5*^{Ctsk} relative to *Chmp5*$^{Ctsk/+}$ periskeletal progenitors. (**D**) Quantitative PCR
1235 determining expression of *H2afx* and *Trp53* genes in *Chmp5*^{Ctsk} relative to *Chmp5*$^{Ctsk/+}$
1236 periskeletal progenitors. *n* = 6 with cells from different animals per group. Data shown as
1237 mean ± s.d.; two-tailed unpaired Student's *t*-test.

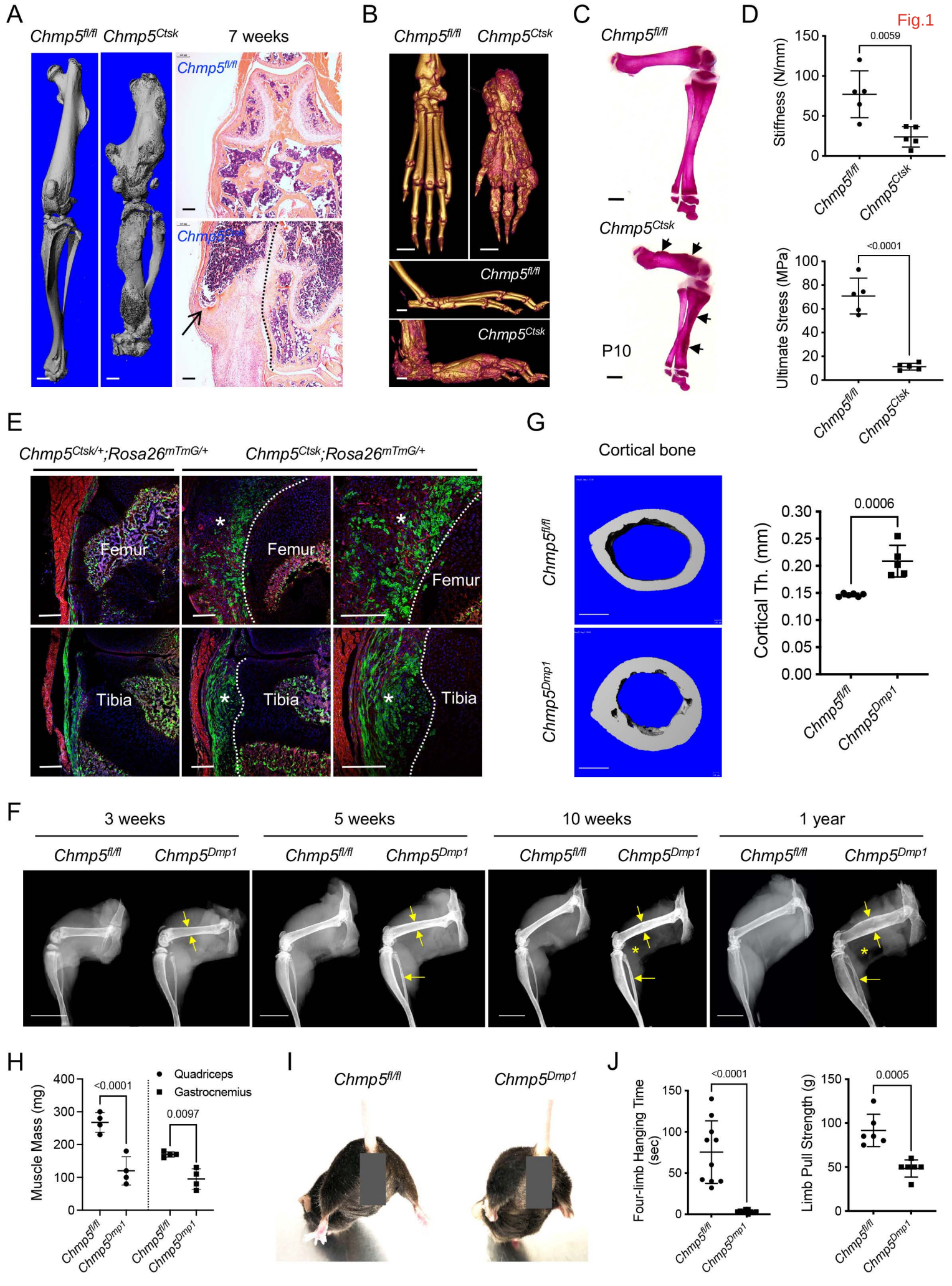
Fig.1
A
Chmp5fl/fl Chmp5Ctsk
7 weeks
Chmp5fl/fl
Chmp5Ctsk
B
Chmp5fl/fl Chmp5Ctsk
Chmp5fl/fl
Chmp5Ctsk
C
Chmp5fl/fl
Chmp5Ctsk
P10
D
Stiffness (N/mm)
0.0059
Chmp5fl/fl
Chmp5Ctsk
Ultimate Stress (MPa)
<0.0001
Chmp5fl/fl
Chmp5Ctsk
E
Chmp5Ctsk/+;Rosa26mTmG/+
Chmp5Ctsk;Rosa26mTmG/+
Femur
Tibia
G
Cortical bone
Chmp5fl/fl
Chmp5Dmp1
Cortical Th. (mm)
0.0006
Chmp5fl/fl
Chmp5Dmp1
F
3 weeks
5 weeks
10 weeks
1 year
Chmp5fl/fl
Chmp5Dmp1
H
Muscle Mass (mg)
Quadriceps
Gastrocnemius
<0.0001
0.0097
Chmp5fl/fl
Chmp5Dmp1
I
Chmp5fl/fl
Chmp5Dmp1
J
Four-limb Hanging Time (sec)
<0.0001
Chmp5fl/fl
Chmp5Dmp1
Limb Pull Strength (g)
0.0005
Chmp5fl/fl
Chmp5Dmp1

Fig. S1

A

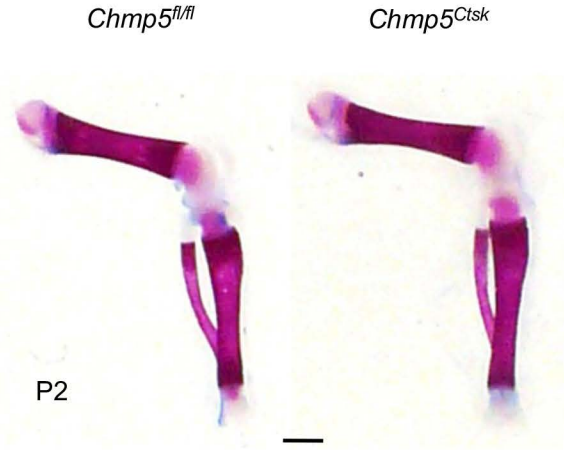
Chmp5fl/fl
Chmp5Ctsk
P2

B

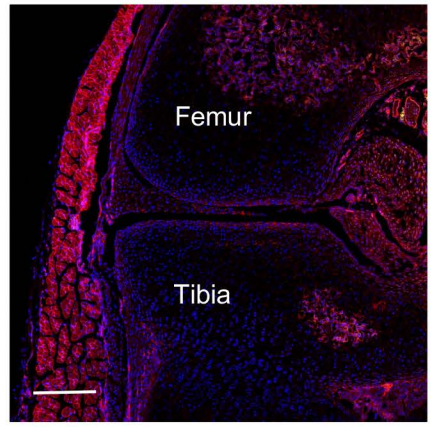
Cre negative control
Femur
Tibia

C

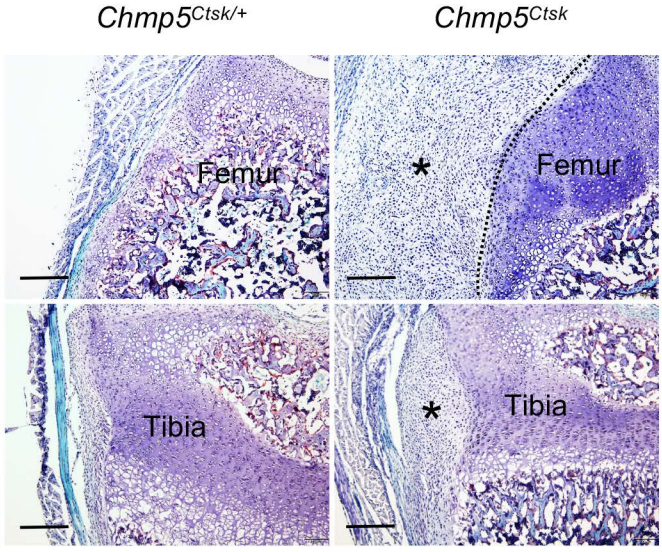
Chmp5Ctsk/+
Chmp5Ctsk
Femur
Femur
*
Tibia
Tibia
*

D

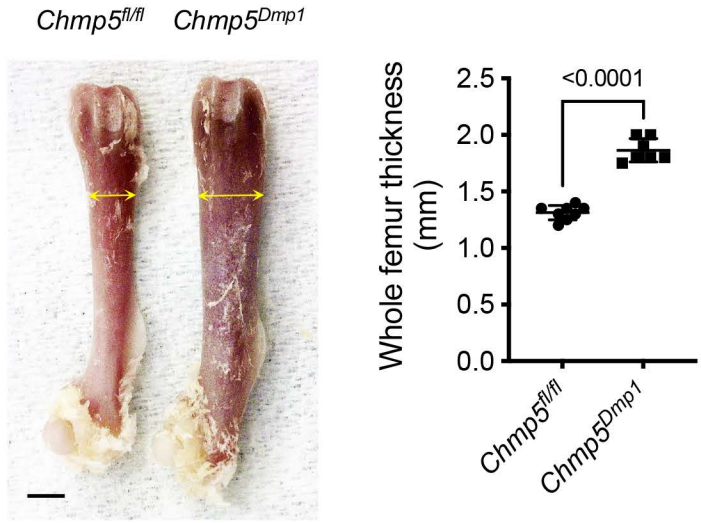
Chmp5fl/fl
Chmp5Dmp1
Whole femur thickness (mm)
2.5
2.0
1.5
1.0
0.5
0.0
<0.0001
Chmp5fl/fl
Chmp5Dmp1

E

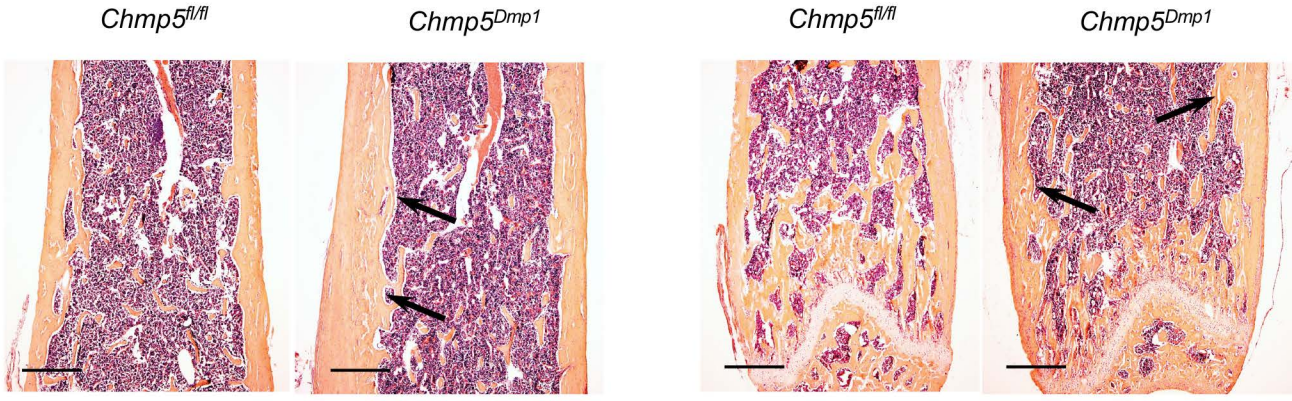
Chmp5fl/fl
Chmp5Dmp1
Chmp5fl/fl
Chmp5Dmp1

A

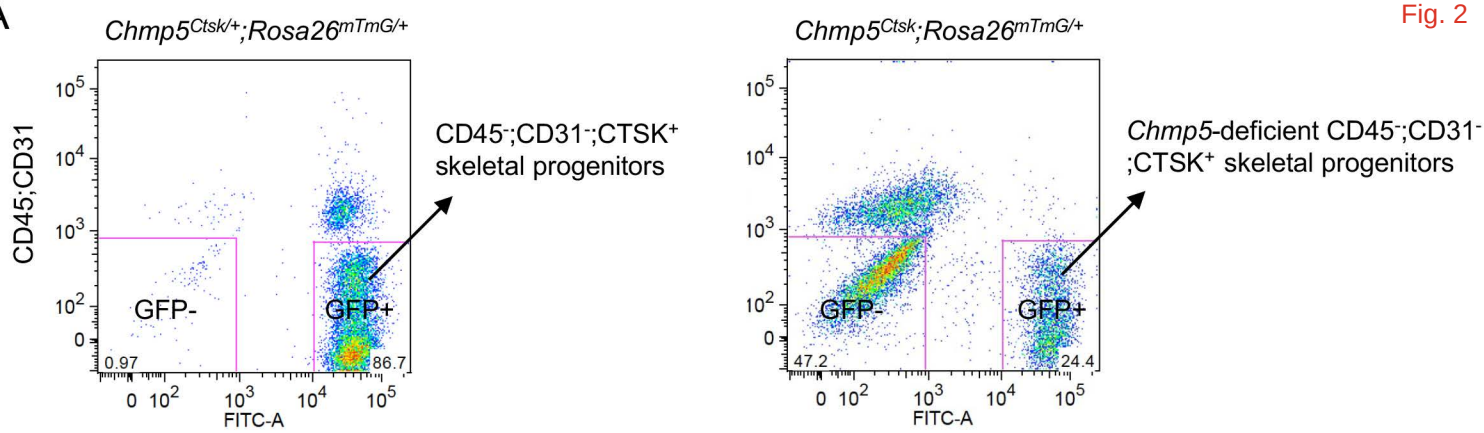

B

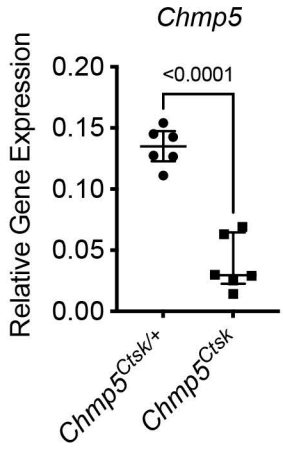

C

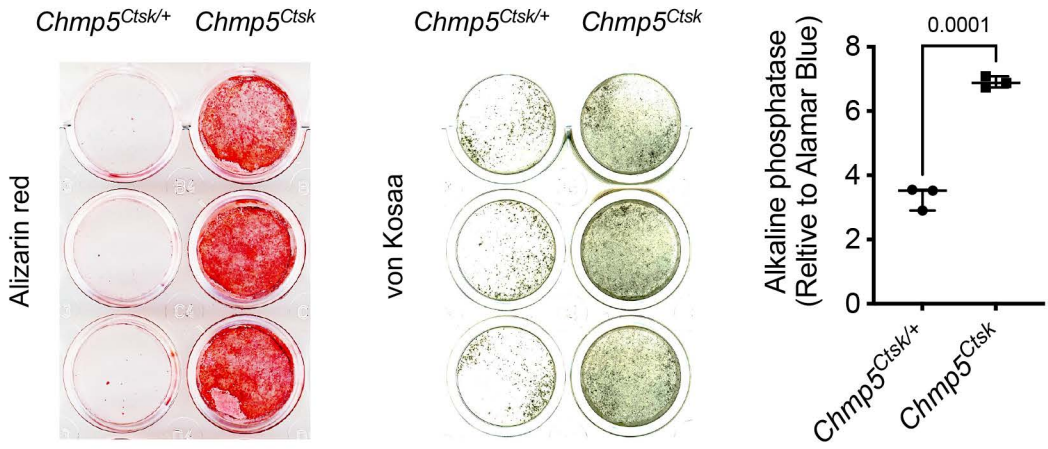

D

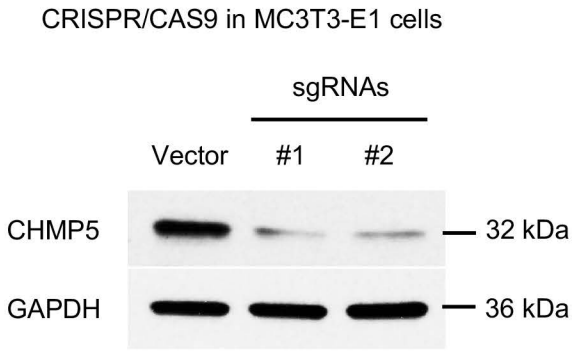

E

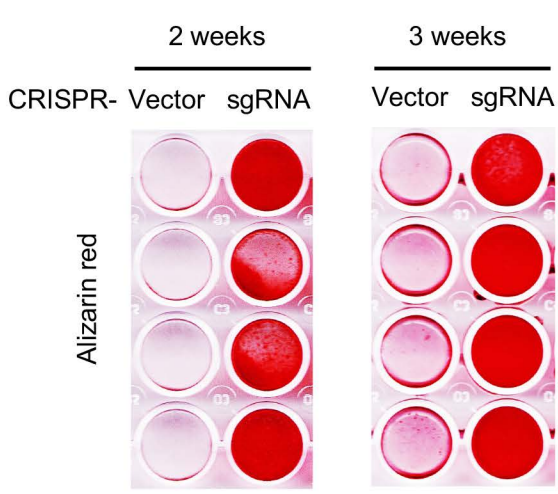

F

Ingenuity pathway analysis of RNA-seq data (*Chmp5*^{Ctsk} vs. *Chmp5*$^{Ctsk/+}$)

Diseases or Functions Annotation	p-Value	Predicted Activation State	Activation z-score	# Molecules
Differentiation of osteoblastic-lineage cells	0.00000101	**Increased**	2.365	44
Differentiation of bone	6.05E-11	**Increased**	2.229	71
Differentiation of osteoblasts	0.00000197	**Increased**	2.101	43
Differentiation of bone cells	1.05E-10	**Increased**	2.1	70

A

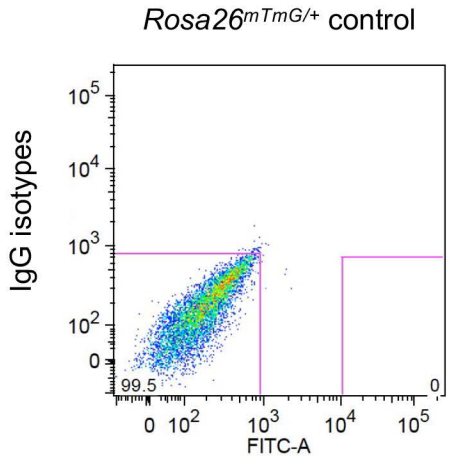
Rosa26mTmG/+ control
IgG isotypes
FITC-A
99.5
0

B

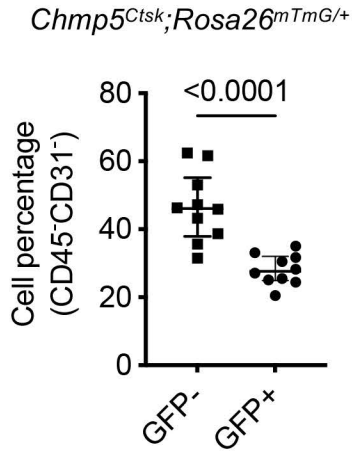
Chmp5Ctsk;Rosa26mTmG/+
<0.0001
Cell percentage (CD45-CD31-)
GFP-
GFP+

A

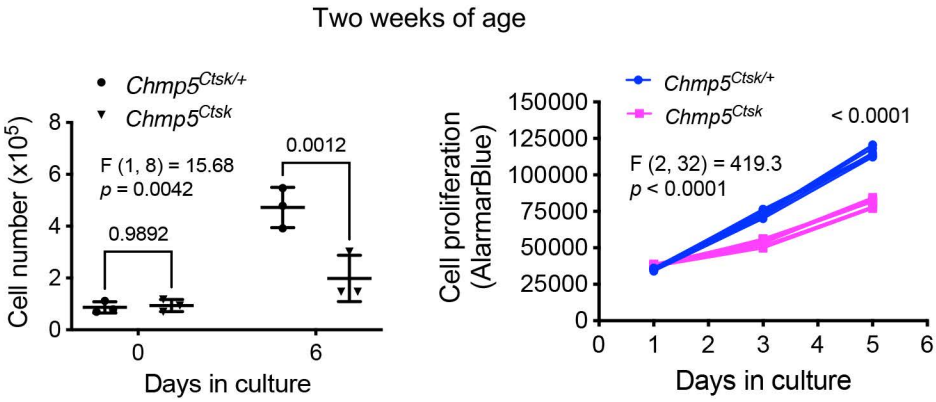
Two weeks of age
Chmp5Ctsk/+
Chmp5Ctsk
Cell number (x10^5)
F (1, 8) = 15.68
p = 0.0042
0.0012
0.9892
Days in culture
Cell proliferation (AlamarBlue)
< 0.0001
F (2, 32) = 419.3
p < 0.0001
Days in culture

B

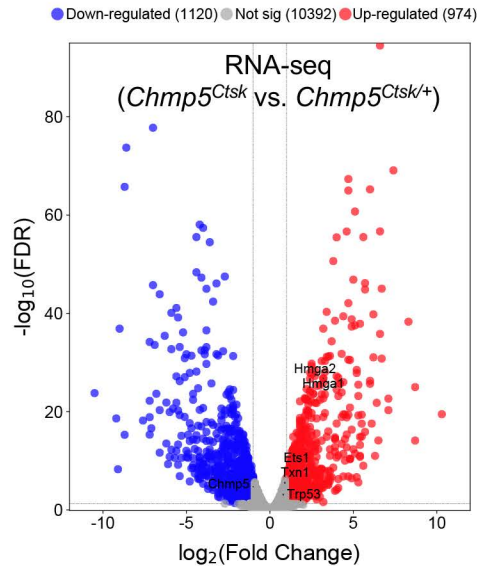
Down-regulated (1120) Not sig (10392) Up-regulated (974)
RNA-seq
(Chmp5Ctsk vs. Chmp5Ctsk/+)
-log10(FDR)
log2(Fold Change)
Hmga2
Hmga1
Ets1
Txn1
Trp53
Chmp5

C

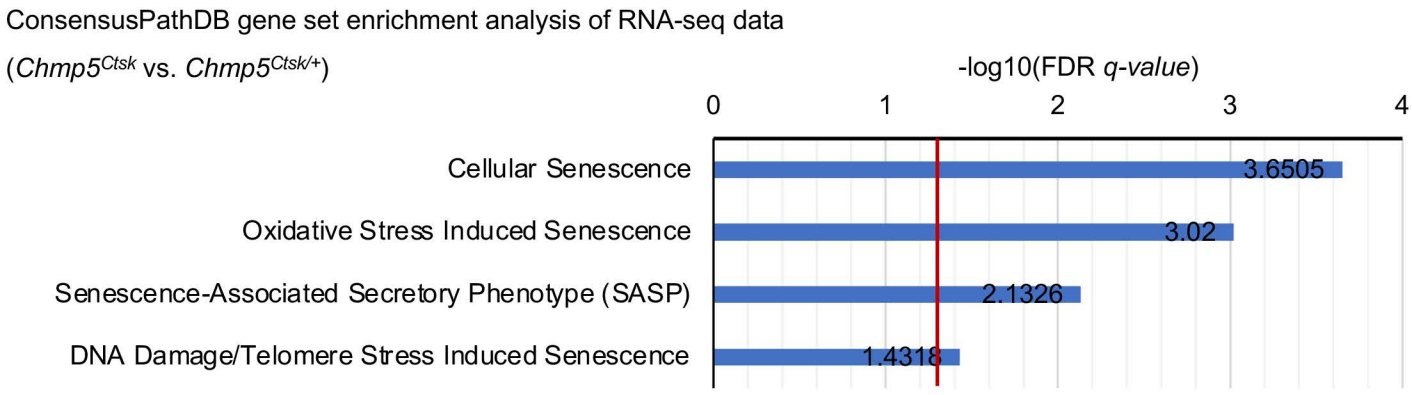
ConsensusPathDB gene set enrichment analysis of RNA-seq data
(Chmp5Ctsk vs. Chmp5Ctsk/+)
-log10(FDR q-value)
Cellular Senescence
3.6505
Oxidative Stress Induced Senescence
3.02
Senescence-Associated Secretory Phenotype (SASP)
2.1326
DNA Damage/Telomere Stress Induced Senescence
1.4318

D

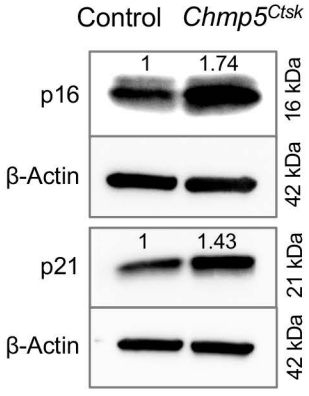
Control
Chmp5Ctsk
p16
1
1.74
16 kDa
β-Actin
42 kDa
p21
1
1.43
21 kDa
β-Actin
42 kDa

E

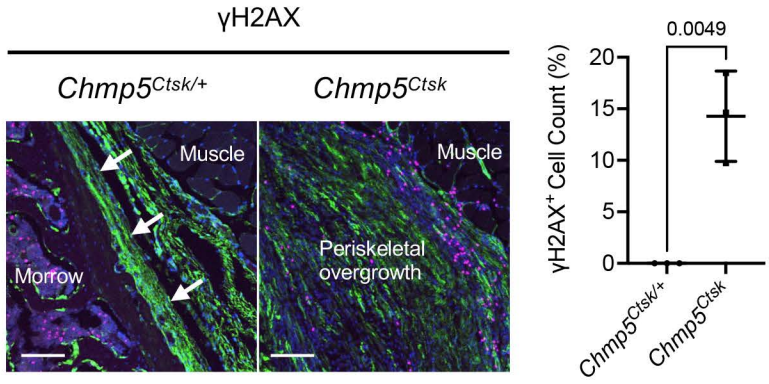
γH2AX
Chmp5Ctsk/+
Chmp5Ctsk
Muscle
Muscle
Morrow
Periskeletal overgrowth
0.0049
γH2AX+ Cell Count (%)
Chmp5Ctsk/+
Chmp5Ctsk

F

Chmp5Ctsk/+
Chmp5Ctsk

G

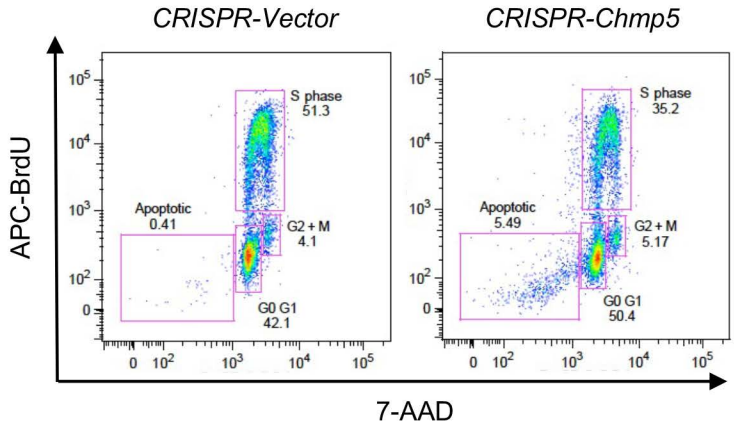
CRISPR-Vector
CRISPR-Chmp5
APC-BrdU
7-AAD
S phase
51.3
Apoptotic
0.41
G2 + M
4.1
G0 G1
42.1
S phase
35.2
Apoptotic
5.49
G2 + M
5.17
G0 G1
50.4

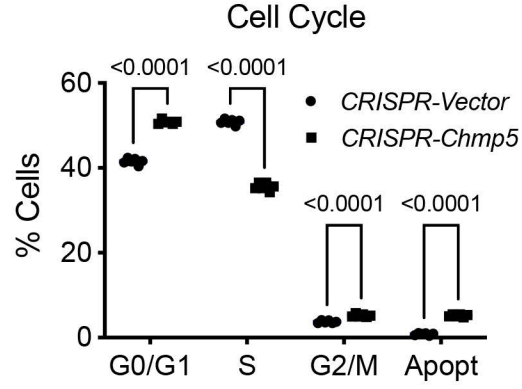
Cell Cycle
<0.0001
<0.0001
CRISPR-Vector
CRISPR-Chmp5
% Cells
<0.0001
<0.0001
G0/G1
S
G2/M
Apopt

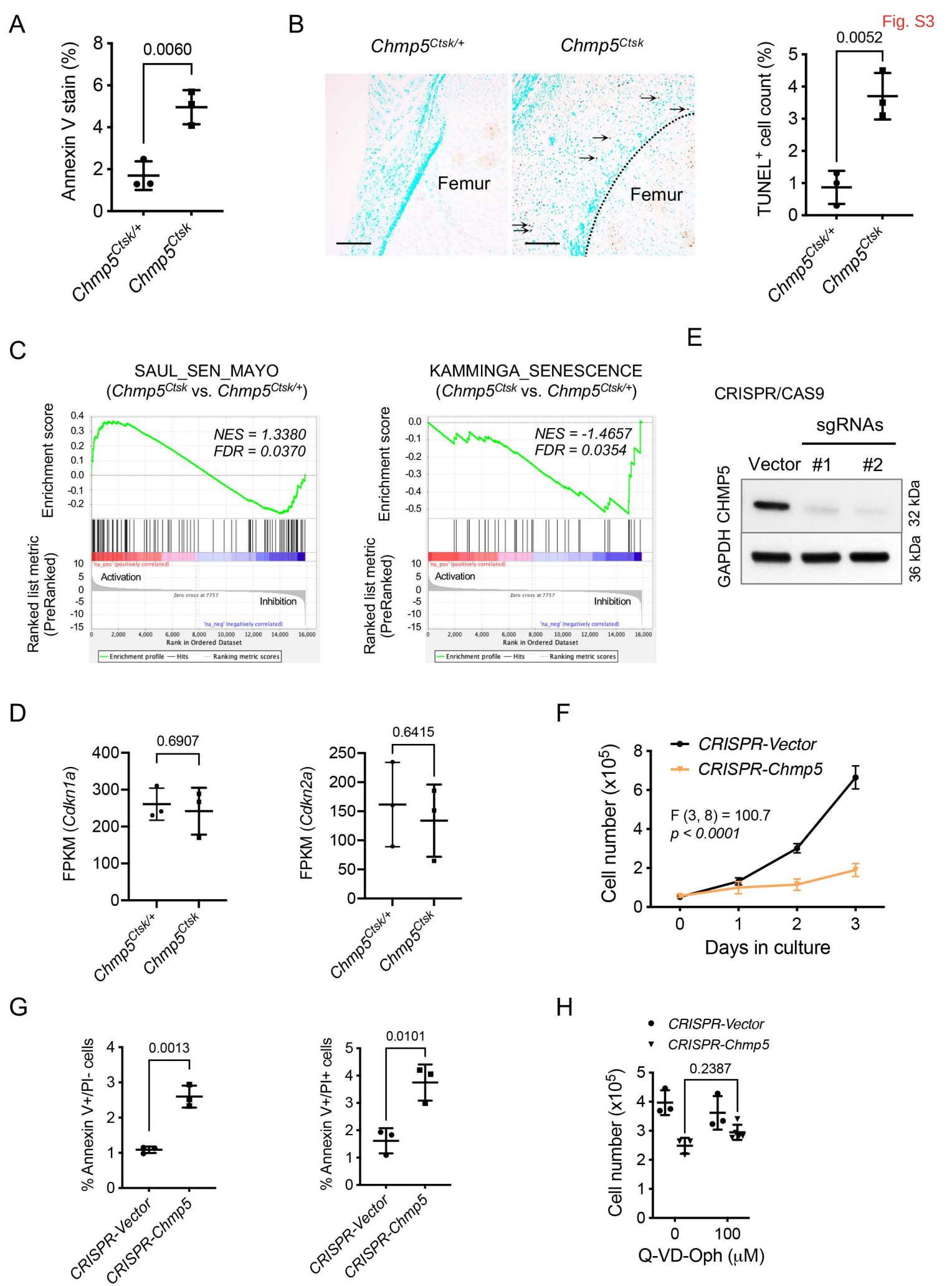
A
Annexin V stain (%)
0.0060
Chmp5Ctsk/+
Chmp5Ctsk
B
Chmp5Ctsk/+
Chmp5Ctsk
Femur
Femur
TUNEL+ cell count (%)
0.0052
C
SAUL_SEN_MAYO
(Chmp5Ctsk vs. Chmp5Ctsk/+)
NES = 1.3380
FDR = 0.0370
KAMMINGA_SENESCENCE
(Chmp5Ctsk vs. Chmp5Ctsk/+)
NES = -1.4657
FDR = 0.0354
Enrichment score
Ranked list metric (PreRanked)
Activation
Inhibition
Rank in Ordered Dataset
Enrichment profile
Hits
Ranking metric scores
E
CRISPR/CAS9
sgRNAs
Vector
#1
#2
GAPDH CHMP5
32 kDa
36 kDa
D
FPKM (Cdkn1a)
0.6907
FPKM (Cdkn2a)
0.6415
F
CRISPR-Vector
CRISPR-Chmp5
Cell number (x10^5)
F (3, 8) = 100.7
p < 0.0001
Days in culture
G
% Annexin V+/PI- cells
0.0013
% Annexin V+/PI+ cells
0.0101
CRISPR-Vector
CRISPR-Chmp5
H
CRISPR-Vector
CRISPR-Chmp5
Cell number (x10^5)
0.2387
Q-VD-Oph (μM)

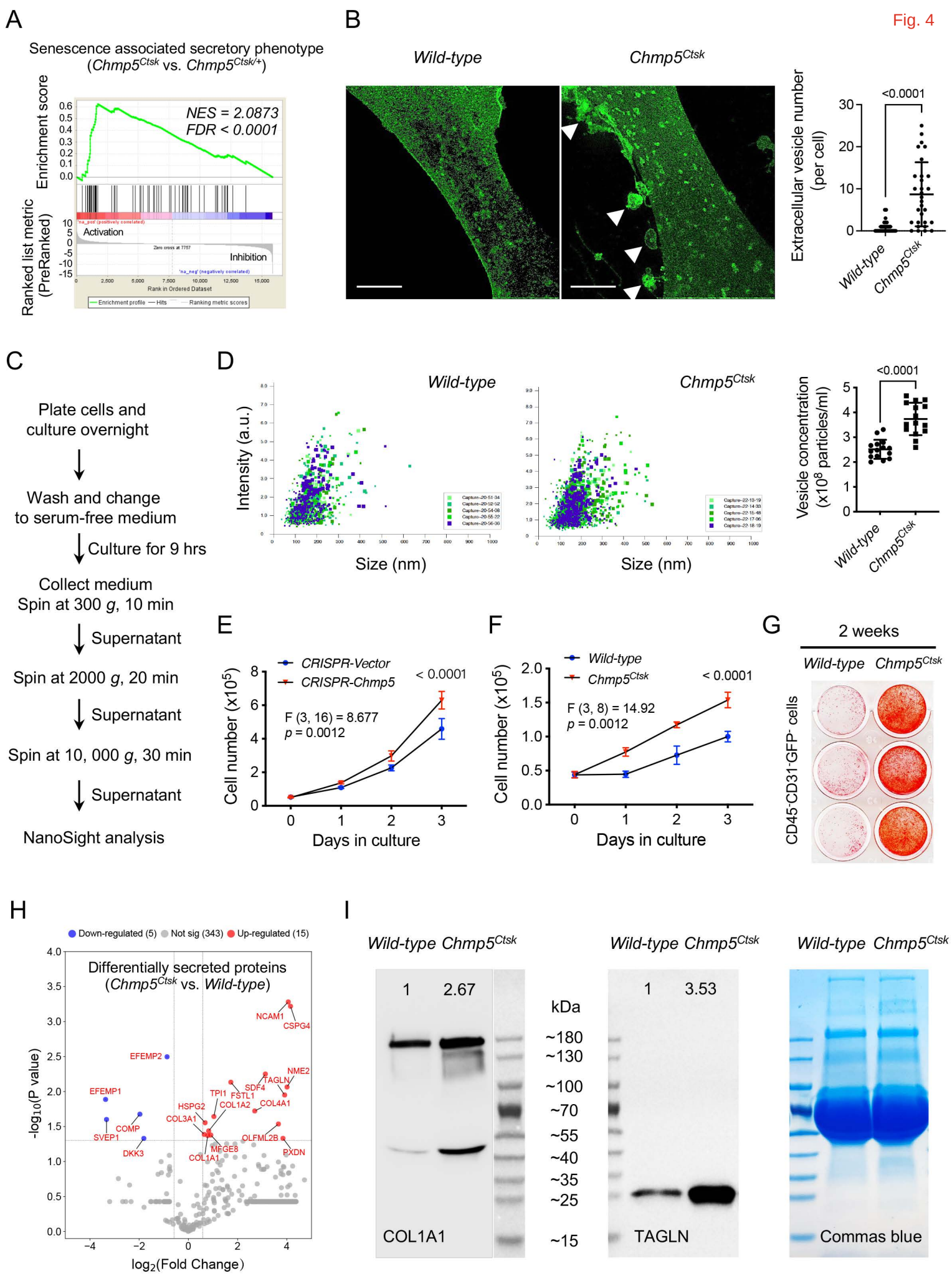
A
Senescence associated secretory phenotype
(Chmp5Ctsk vs. Chmp5Ctsk/+)
Enrichment score
NES = 2.0873
FDR < 0.0001
Ranked list metric
(PreRanked)
Activation
Inhibition
Rank in Ordered Dataset
Enrichment profile
Hits
Ranking metric scores
B
Wild-type
Chmp5Ctsk
Extracellular vesicle number
(per cell)
<0.0001
Wild-type
Chmp5Ctsk
C
Plate cells and
culture overnight
Wash and change
to serum-free medium
Culture for 9 hrs
Collect medium
Spin at 300 g, 10 min
Supernatant
Spin at 2000 g, 20 min
Supernatant
Spin at 10, 000 g, 30 min
Supernatant
NanoSight analysis
D
Wild-type
Chmp5Ctsk
Intensity (a.u.)
Size (nm)
Vesicle concentration
(x10^8 particles/ml)
<0.0001
Wild-type
Chmp5Ctsk
E
CRISPR-Vector
CRISPR-Chmp5
< 0.0001
F (3, 16) = 8.677
p = 0.0012
Cell number (x10^5)
Days in culture
F
Wild-type
Chmp5Ctsk
< 0.0001
F (3, 8) = 14.92
p = 0.0012
Cell number (x10^5)
Days in culture
G
2 weeks
Wild-type
Chmp5Ctsk
CD45-CD31-GFP- cells
H
Down-regulated (5)
Not sig (343)
Up-regulated (15)
Differentially secreted proteins
(Chmp5Ctsk vs. Wild-type)
NCAM1
CSPG4
EFEMP2
NME2
TAGLN
SDF4
EFEMP1
TPI1
FSTL1
HSPG2
COL1A2
COL4A1
COL3A1
COMP
SVEP1
OLFML2B
DKK3
MFGE8
PXDN
COL1A1
-log10(P value)
log2(Fold Change)
I
Wild-type
Chmp5Ctsk
1
2.67
kDa
~180
~130
~100
~70
~55
~40
~35
~25
~15
COL1A1
Wild-type
Chmp5Ctsk
1
3.53
TAGLN
Wild-type
Chmp5Ctsk
Commas blue

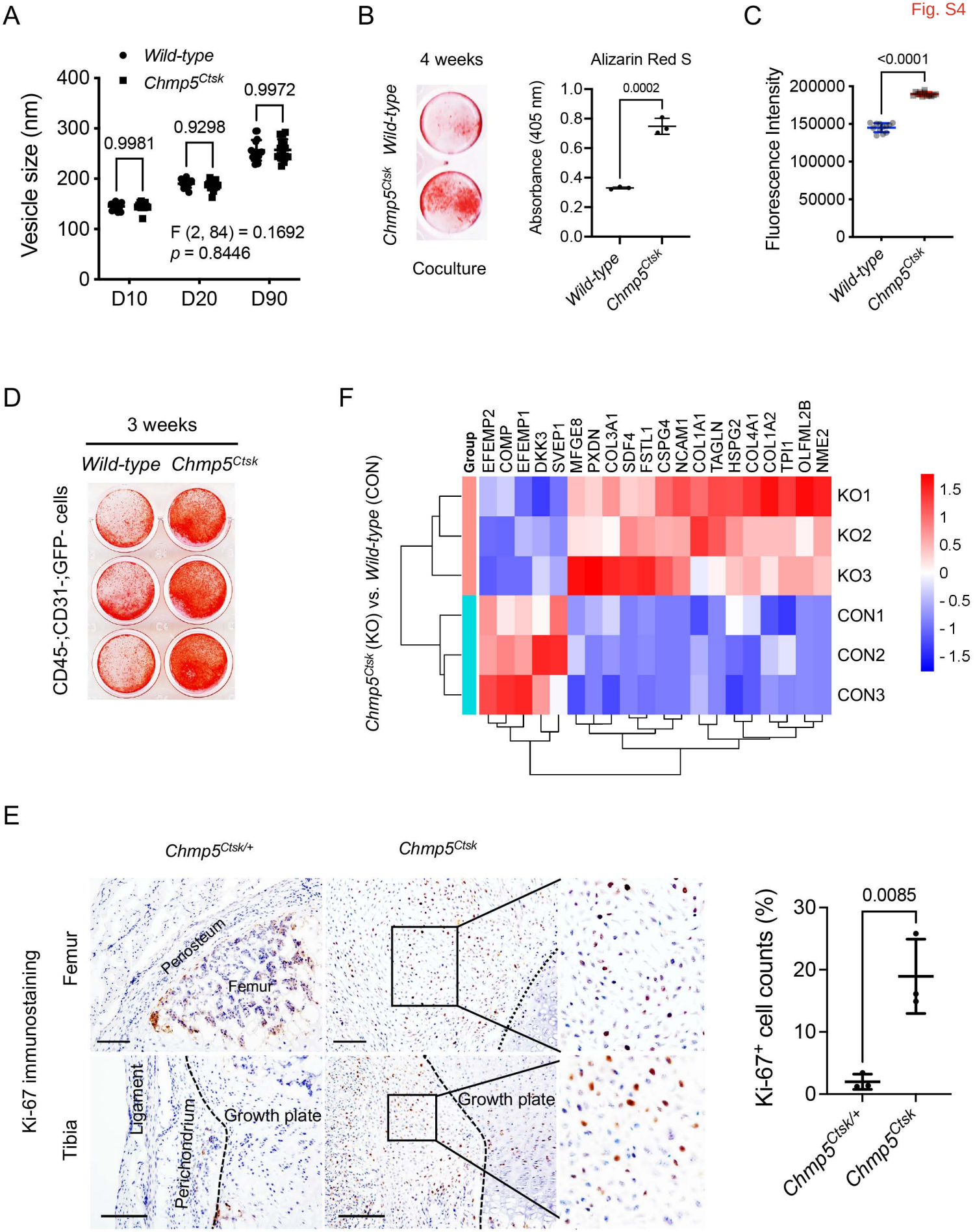
A
Wild-type
Chmp5Ctsk
Vesicle size (nm)
400
300
200
100
0
0.9981
0.9298
0.9972
F (2, 84) = 0.1692
p = 0.8446
D10
D20
D90
B
4 weeks
Alizarin Red S
Wild-type
Chmp5Ctsk
Coculture
Absorbance (405 nm)
1.0
0.8
0.6
0.4
0.2
0.0
0.0002
Wild-type
Chmp5Ctsk
C
<0.0001
Fluorescence Intensity
200000
150000
100000
50000
0
Wild-type
Chmp5Ctsk
D
3 weeks
Wild-type
Chmp5Ctsk
CD45-;CD31-;GFP- cells
F
Group
EFEMP2
COMP
EFEMP1
DKK3
SVEP1
MFGE8
PXDN
COL3A1
SDF4
FSTL1
CSPG4
NCAM1
COL1A1
TAGLN
HSPG2
COL4A1
COL1A2
TPI1
OLFML2B
NME2
Chmp5Ctsk (KO) vs. Wild-type (CON)
KO1
KO2
KO3
CON1
CON2
CON3
1.5
1
0.5
0
- 0.5
- 1
- 1.5
E
Chmp5Ctsk/+
Chmp5Ctsk
Ki-67 immunostaining
Femur
Tibia
Periosteum
Femur
Ligament
Perichondrium
Growth plate
Growth plate
Ki-67+ cell counts (%)
30
20
10
0
0.0085
Chmp5Ctsk/+
Chmp5Ctsk

A

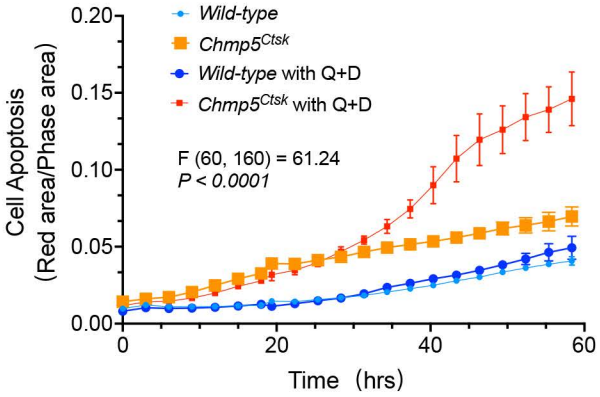
Wild-type
Chmp5Ctsk
Wild-type with Q+D
Chmp5Ctsk with Q+D
F (60, 160) = 61.24
P < 0.0001
Cell Apoptosis
(Red area/Phase area)
Time (hrs)
0.20
0.15
0.10
0.05
0.00
0
20
40
60

C

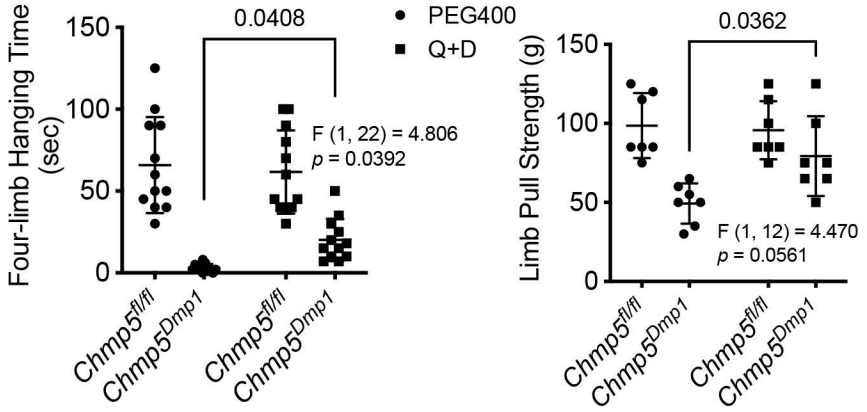
Four-limb Hanging Time (sec)
0.0408
PEG400
Q+D
F (1, 22) = 4.806
p = 0.0392
Limb Pull Strength (g)
0.0362
F (1, 12) = 4.470
p = 0.0561
Chmp5fl/fl
Chmp5Dmp1
150
100
50
0

B

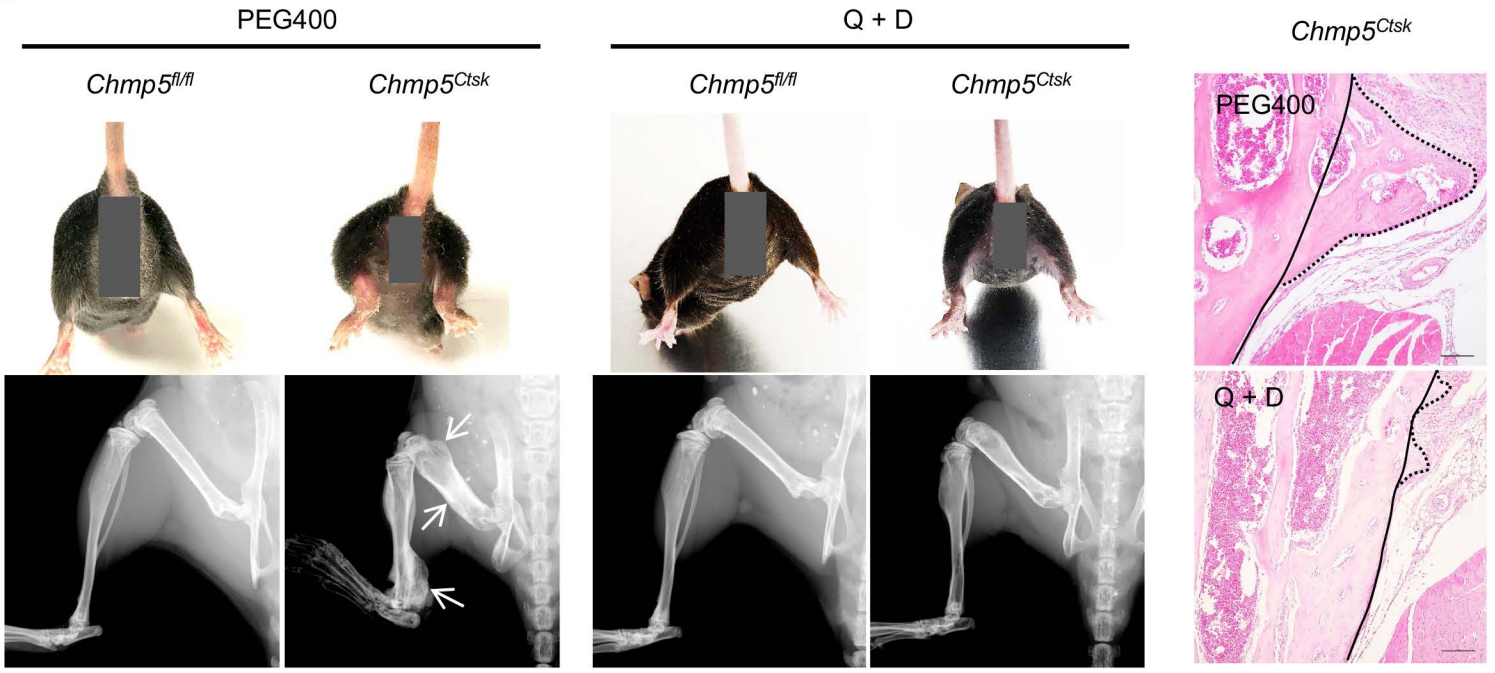
PEG400
Q + D
Chmp5fl/fl
Chmp5Ctsk
Chmp5Ctsk
PEG400
Q + D

D

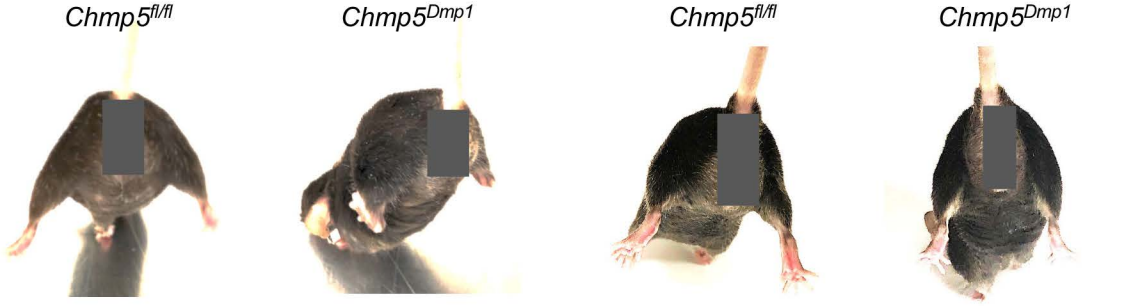
PEG400
Q + D
Chmp5fl/fl
Chmp5Dmp1

E

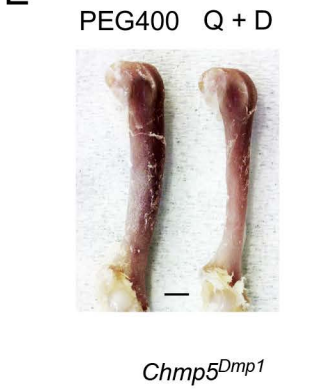
PEG400
Q + D
Chmp5Dmp1
0.0017
Cortical Th. (mm)
0.30
0.25
0.20
0.15
0.10
0.05
0.00
PEG400
Q+D

F

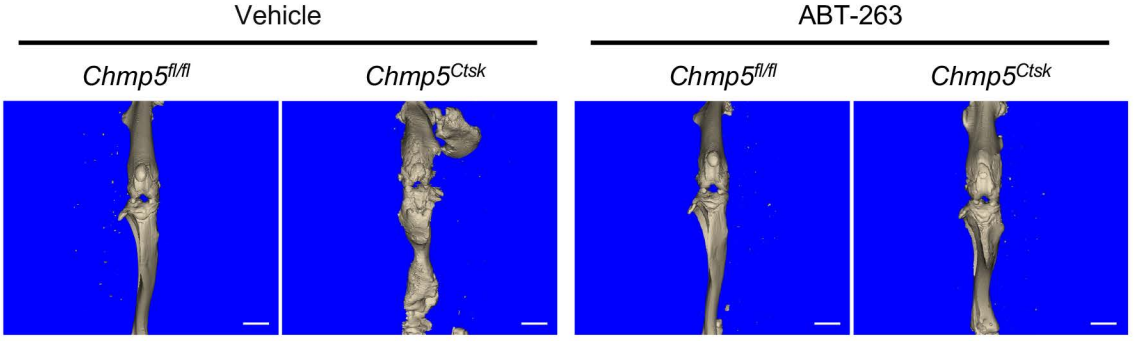
Vehicle
ABT-263
Chmp5fl/fl
Chmp5Ctsk

Chmp5^{Ctsk}

Fig. S5

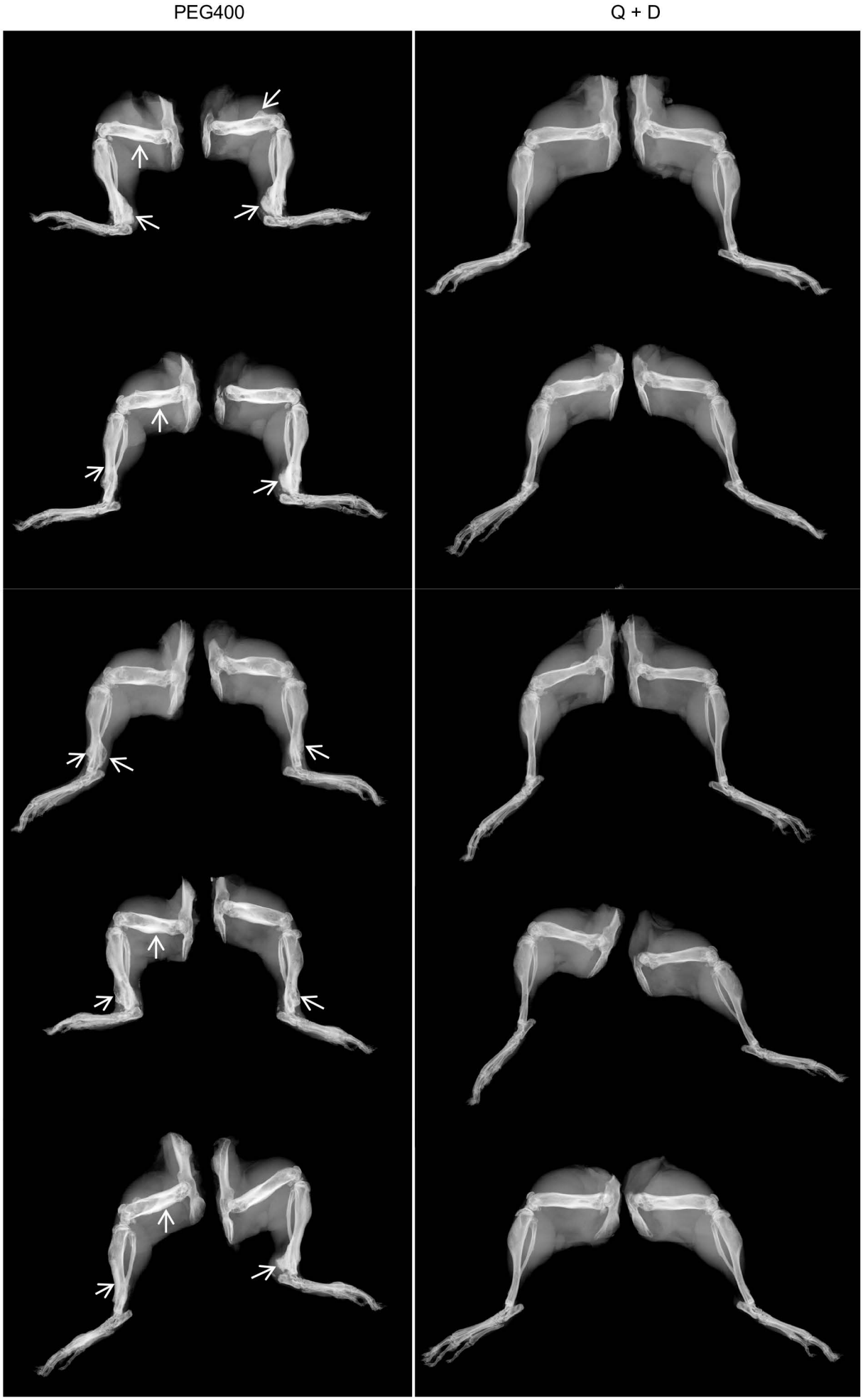

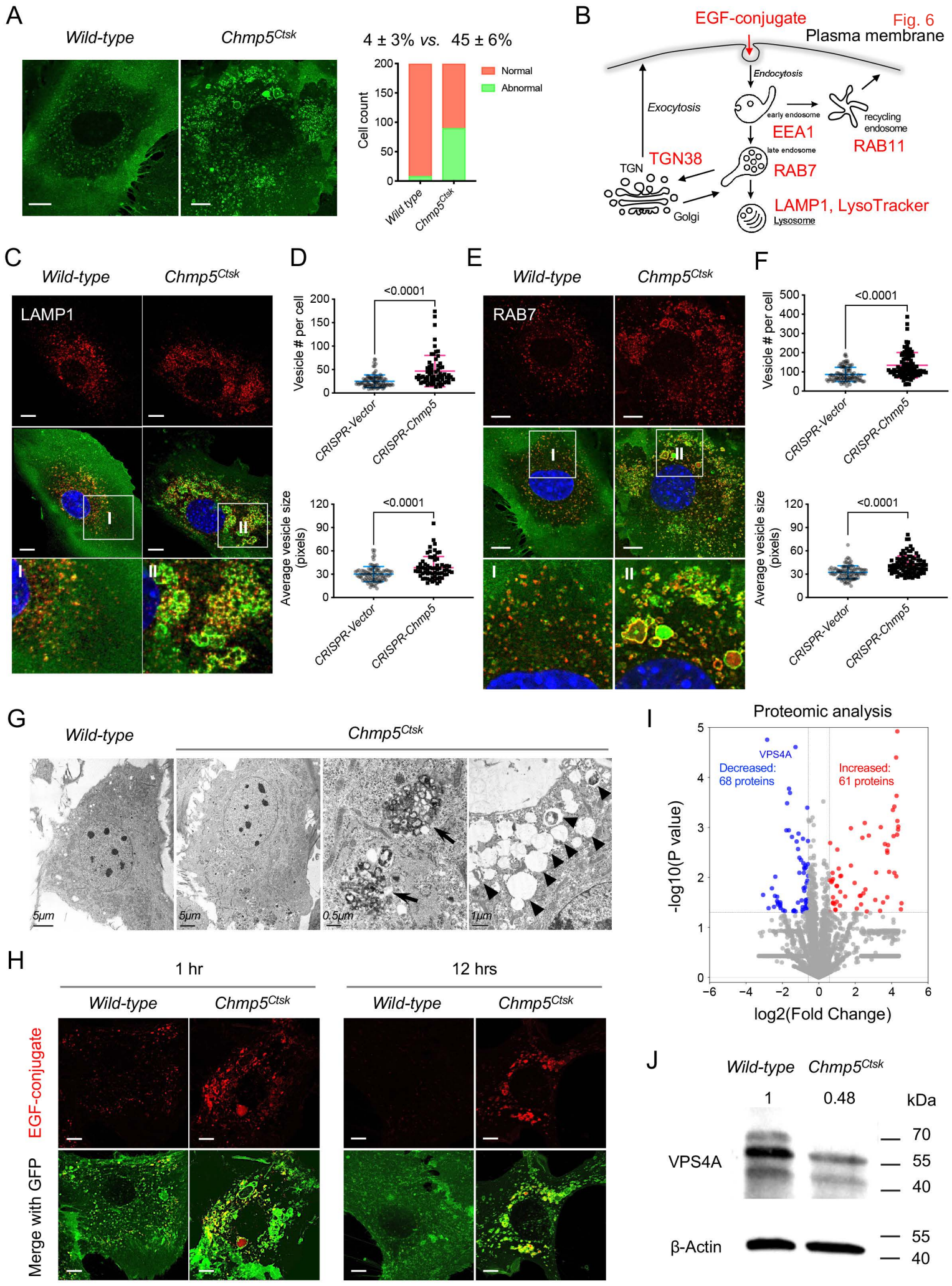
A
Wild-type
Chmp5Ctsk
4 ± 3% vs. 45 ± 6%
Cell count
Normal
Abnormal
Wild type
Chmp5Ctsk
B
EGF-conjugate
Fig. 6
Plasma membrane
Endocytosis
Exocytosis
early endosome
EEA1
recycling endosome
RAB11
late endosome
RAB7
TGN
TGN38
Golgi
LAMP1, LysoTracker
Lysosome
C
Wild-type
Chmp5Ctsk
LAMP1
D
Vesicle # per cell
<0.0001
CRISPR-Vector
CRISPR-Chmp5
Average vesicle size (pixels)
E
Wild-type
Chmp5Ctsk
RAB7
F
Vesicle # per cell
<0.0001
Average vesicle size (pixels)
G
Wild-type
Chmp5Ctsk
5μm
0.5μm
1μm
H
1 hr
12 hrs
Wild-type
Chmp5Ctsk
EGF-conjugate
Merge with GFP
I
Proteomic analysis
VPS4A
Decreased: 68 proteins
Increased: 61 proteins
-log10(P value)
log2(Fold Change)
J
Wild-type
Chmp5Ctsk
1
0.48
kDa
VPS4A
β-Actin
70
55
40
55
40

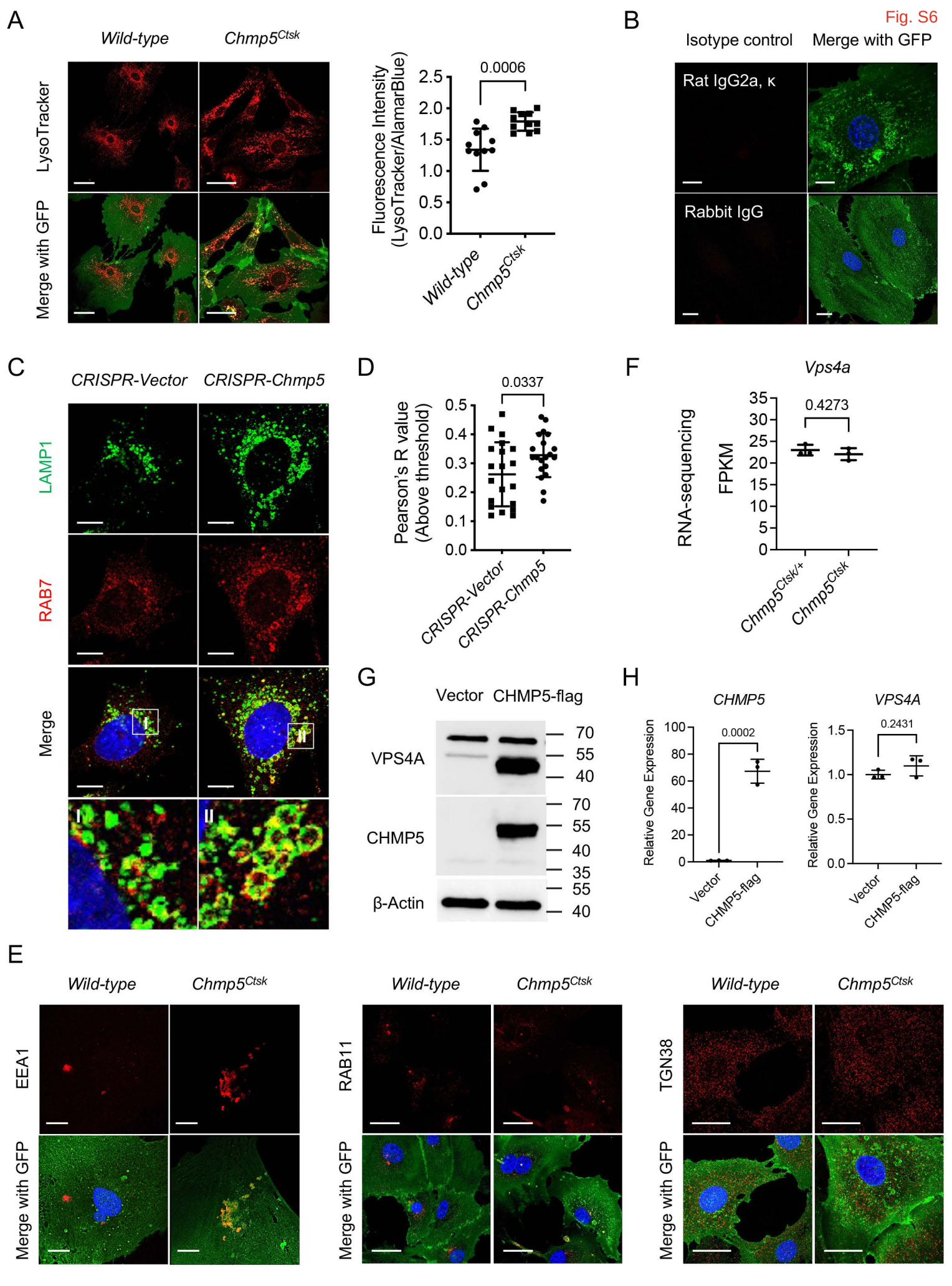
A
Wild-type
Chmp5Ctsk
LysoTracker
Merge with GFP
Fluorescence Intensity (LysoTracker/AlamarBlue)
0.0006
2.5
2.0
1.5
1.0
0.5
0.0
Wild-type
Chmp5Ctsk
B
Isotype control
Merge with GFP
Rat IgG2a, κ
Rabbit IgG
C
CRISPR-Vector
CRISPR-Chmp5
LAMP1
RAB7
Merge
I
II
D
Pearson's R value (Above threshold)
0.0337
0.5
0.4
0.3
0.2
0.1
0.0
CRISPR-Vector
CRISPR-Chmp5
F
Vps4a
RNA-sequencing
FPKM
0.4273
35
30
25
20
15
10
5
0
Chmp5Ctsk/+
Chmp5Ctsk
G
Vector
CHMP5-flag
VPS4A
CHMP5
β-Actin
70
55
40
70
55
40
35
55
40
H
CHMP5
VPS4A
Relative Gene Expression
0.0002
0.2431
100
80
60
40
20
0
1.5
1.0
0.5
0.0
Vector
CHMP5-flag
E
Wild-type
Chmp5Ctsk
EEA1
RAB11
TGN38
Merge with GFP

A

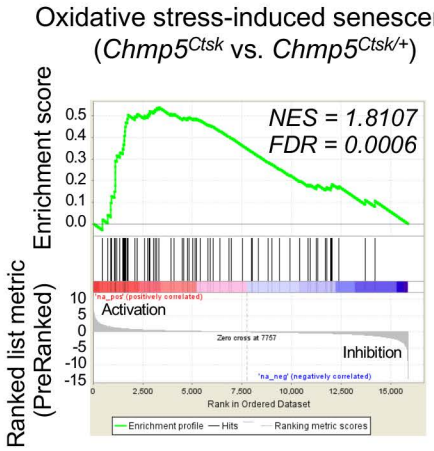
Oxidative stress-induced senescence
(Chmp5Ctsk vs. Chmp5Ctsk/+)
Enrichment score
NES = 1.8107
FDR = 0.0006
Ranked list metric
(PreRanked)
Activation
Inhibition
Rank in Ordered Dataset
Enrichment profile
Hits
Ranking metric scores

B

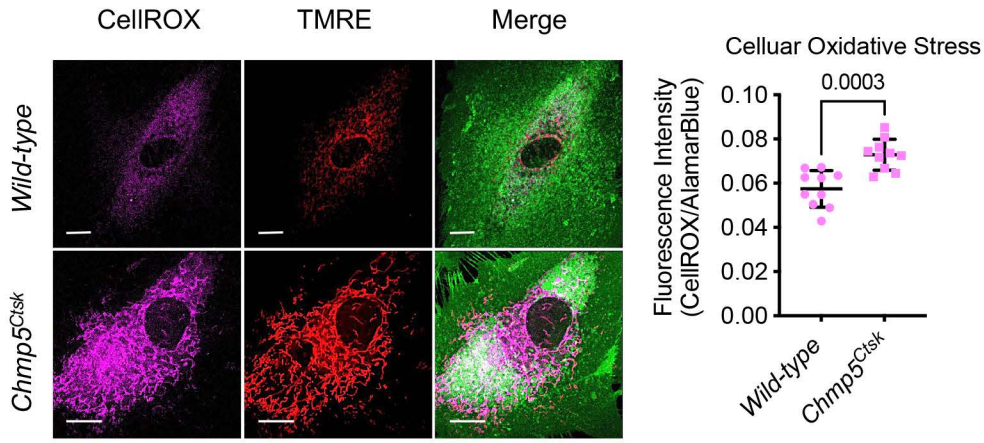
CellROX
TMRE
Merge
Wild-type
Chmp5Ctsk
Celluar Oxidative Stress
0.0003
Fluorescence Intensity
(CellROX/AlamarBlue)
Wild-type
Chmp5Ctsk

C

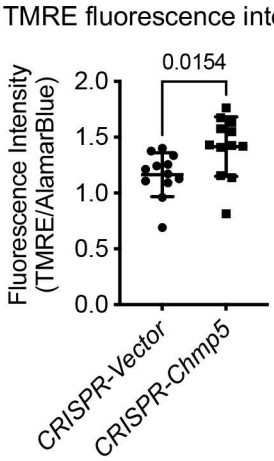
TMRE fluorescence intensity
0.0154
Fluorescence Intensity
(TMRE/AlamarBlue)
CRISPR-Vector
CRISPR-Chmp5

D

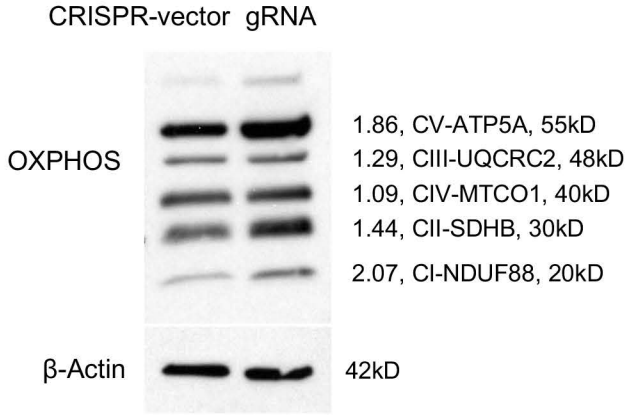
CRISPR-vector gRNA
OXPHOS
1.86, CV-ATP5A, 55kD
1.29, CIII-UQCRC2, 48kD
1.09, CIV-MTCO1, 40kD
1.44, CII-SDHB, 30kD
2.07, CI-NDUF88, 20kD
β-Actin
42kD

E

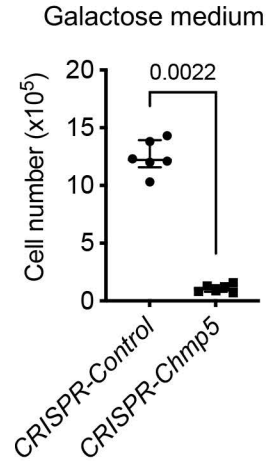
Galactose medium
0.0022
Cell number (x10^5)
CRISPR-Control
CRISPR-Chmp5

F

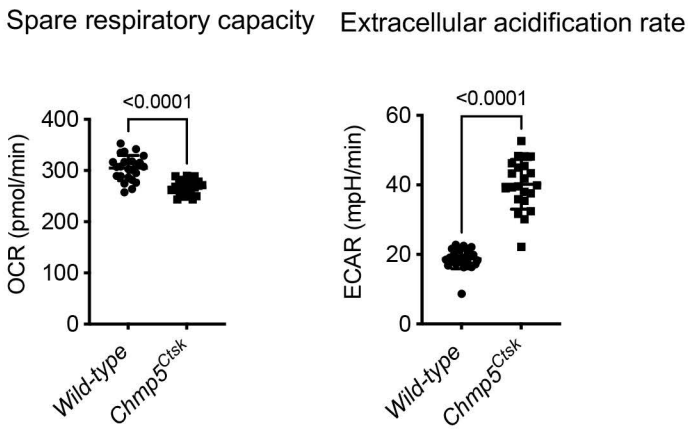
Spare respiratory capacity
<0.0001
OCR (pmol/min)
Wild-type
Chmp5Ctsk
Extracellular acidification rate
<0.0001
ECAR (mpH/min)
Wild-type
Chmp5Ctsk

G

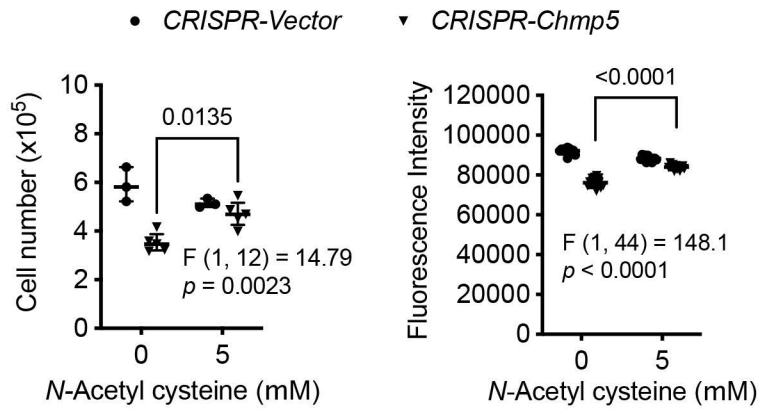
CRISPR-Vector
CRISPR-Chmp5
0.0135
Cell number (x10^5)
F (1, 12) = 14.79
p = 0.0023
N-Acetyl cysteine (mM)
<0.0001
Fluorescence Intensity
F (1, 44) = 148.1
p < 0.0001
N-Acetyl cysteine (mM)

H

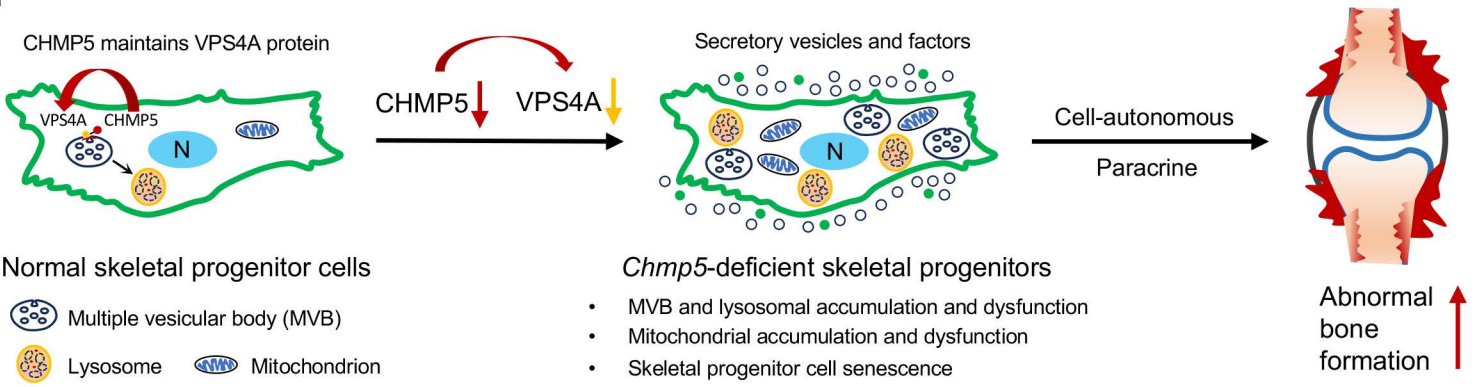
CHMP5 maintains VPS4A protein
VPS4A
CHMP5
N
CHMP5
VPS4A
Secretory vesicles and factors
N
Cell-autonomous
Paracrine
Normal skeletal progenitor cells
Multiple vesicular body (MVB)
Lysosome
Mitochondrion
Chmp5-deficient skeletal progenitors
MVB and lysosomal accumulation and dysfunction
Mitochondrial accumulation and dysfunction
Skeletal progenitor cell senescence
Abnormal
bone
formation

A

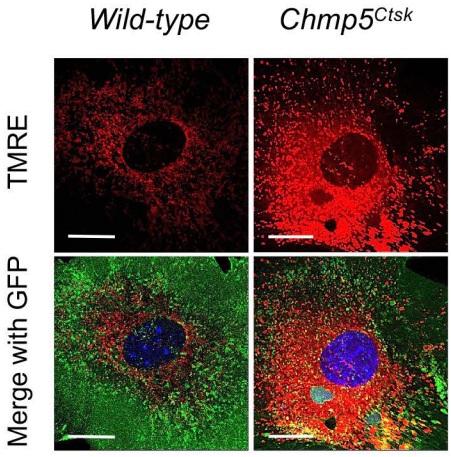
Wild-type
Chmp5Ctsk
TMRE
Merge with GFP

B

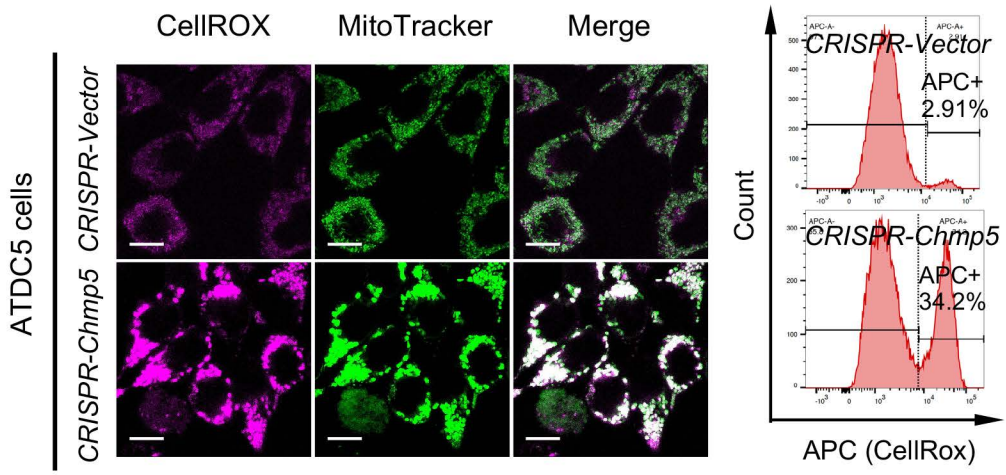
CellROX
MitoTracker
Merge
ATDC5 cells
CRISPR-Vector
CRISPR-Chmp5
CRISPR-Vector
APC+
2.91%
CRISPR-Chmp5
APC+
34.2%
Count
APC (CellRox)

C

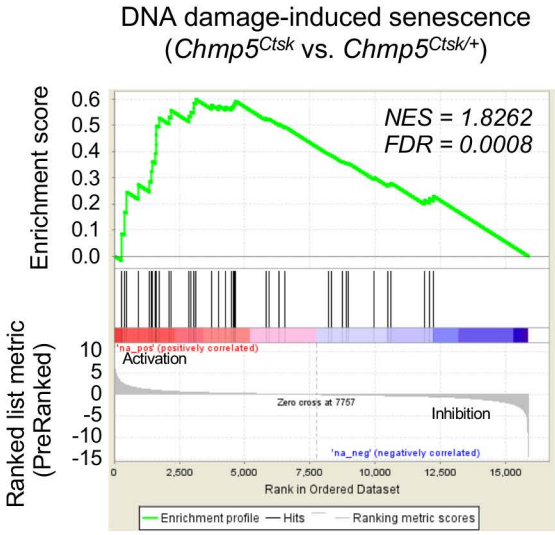
DNA damage-induced senescence
(Chmp5Ctsk vs. Chmp5Ctsk/+)
NES = 1.8262
FDR = 0.0008
Enrichment score
Ranked list metric
(PreRanked)
Activation
Inhibition
Zero cross at 7757
Rank in Ordered Dataset
Enrichment profile
Hits
Ranking metric scores

D

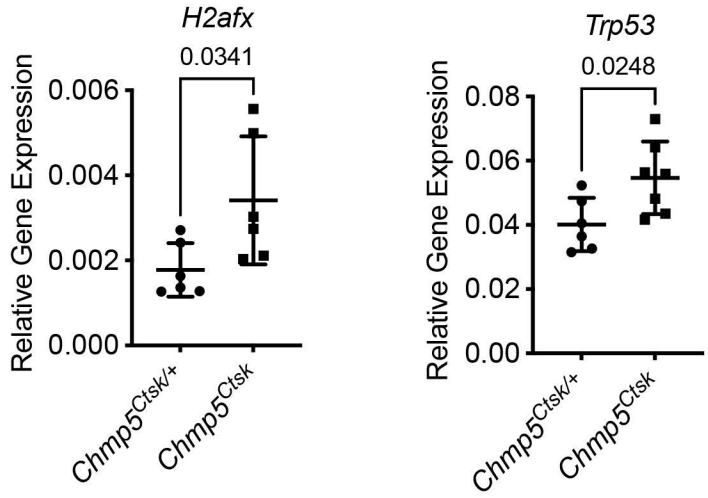
H2afx
0.0341
Relative Gene Expression
Chmp5Ctsk/+
Chmp5Ctsk
Trp53
0.0248
Relative Gene Expression
Chmp5Ctsk/+
Chmp5Ctsk